Phosphorus on platinum surfaces – from molecular adsorption to catalyst poisoning

Olli Heikkinen

Phosphorus on platinum surfaces – from molecular adsorption to catalyst poisoning

Olli Heikkinen

A doctoral dissertation completed for the degree of Doctor of Science (Technology) to be defended, with the permission of the Aalto University School of Science, at a public examination held at the lecture hall M1 of the school on 24 April 2017 at 13.

Aalto University
School of Science
Department of Applied Physics
Surface Science

Supervising professor

Prof. Peter Liljeroth, Aalto University, Finland

Thesis advisor

Dr. Jouko Lahtinen, Aalto University, Finland

Preliminary examiners

Prof. Kalevi Kokko, University of Turku, Finland
Assoc. Prof. Katariina Pussi, Lappeenranta University of Technology, Finland

Opponent

Prof. Georg Held, University of Reading, United Kingdom

NORDIC ECOLABEL

441   697
Printed matter

Abstract

Platinum is a catalytically active metal widely used in technology. An important application is automotive exhaust gas catalysis, aiming at reducing combustion engine emissions. Platinum is used to catalyse oxidation reactions of carbon monoxide and hydrocarbons, for instance. On the other hand, phosphorus is a catalyst poison. It is adsorbed on catalyst surfaces, causing decrease in the catalytic activity. In practice, phosphorus is commonly found in lubricant oils and additives, which makes phosphorus poisoning a true problem in exhaust gas catalysis. In addition to real catalysts, studying phosphorus adsorption on platinum single crystal surfaces may give insight into the mechanism of poisoning. However, so far the number of such studies has remained relatively limited.

   In this work, molecular phosphorus adsorption on platinum (111) and (110) surfaces has been investigated. In addition, effects of phosphorus as well as sulfur on real platinum and platinum-palladium catalysts for diesel and natural gas oxidation have been studied. Furthermore, one section is devoted to maleic anhydride adsorption on platinum (111). Maleic anhydride is an organic molecule, used as an intermediate in many large-scale chemical manufacturing processes, related for instance to lubricant oils and biofuels. The studies featured in this work have been carried out with standard techniques of surface science, such as X-ray photoelectron spectroscopy, low-energy electron diffraction, scanning tunnelling microscopy and temperature-programmed desorption. Furthermore, results acquired with additional experimental and computational methods by collaborators are also reported.

   Phosphorus adsorption on both single crystal surfaces was found to be more efficient on elevated temperatures. Annealing the surface after deposition resulted in formation of ordered structures. Several different superstructures were found, depending on the phosphorus coverage which eventually saturated on both surfaces. Phosphorus was observed to have a tendency towards forming large clusters. On the real catalyst surfaces, phosphorus was found to form phosphate compounds with particles in the catalyst support. It also induced morphological changes, such as decreasing the specific surface areas. The magnitude of deactivation varied from moderate to severe depending on the catalyst and the reaction. Sulfur was found to mitigate the poisoning effect caused by phosphorus. Maleic anhydride formed unordered multilayer structures on platinum (111). All molecules desorbed or dissociated below room temperature, above which desorption of molecule fragments was observed in a wide temperature range. The results gained in this work give insight into how catalyst poisoning induced by phosphorus takes place. Moreover, they also give answers to some previously uncharted problems in fundamental surface science.

Tiivistelmä

Platina on katalyyttisesti aktiivinen metalli, jota käytetään laajasti teollisuudessa. Merkittävä sovellus ovat autojen pakokaasukatalysaattorit, joiden tehtävä on vähentää haitallisia päästöjä. Niissä platinaa käytetään esimerkiksi katalysoimaan hiilimonoksidin ja hiilivetyjen hapetusreaktioita. Fosfori puolestaan on katalyyttimyrkky. Se adsorboituu katalyyttipinnalle ja aiheuttaa tämän aktiivisuuden heikentymistä. Fosfori on yleinen ainesosa voiteluöljyissä ja niiden lisäaineissa, ja siksi fosforimyrkyttyminen on pakokaasukatalyyttien todellinen ongelma. Myrkyttymismekanismien yksityiskohtien ymmärtämiseksi voi olla hyödyllistä tutkia teollisten katalyyttimateriaalien ohella myös fosforin adsorboitumista yksittäiskiteisille platinapinnoille. Toistaiseksi tällaista tutkimusta on kuitenkin tehty varsin rajoitetusti.

Tässä työssä on tutkittu fosforin adsorptiota platina (111) ja (110) -pinnoille. Toisena tutkimuskohteena on ollut fosforin sekä rikin vaikutus eräisiin diesel- ja maakaasuajoneuvokäyttöön valmistettuihin hapetuskatalyytteihin. Näiden lisäksi yksi työn osio käsittelee maleiinianhydridin adsorptiota platina (111) -pinnalle. Maleiinianhydridi on orgaaninen molekyyli, jota käytetään yleisesti kemianteollisuudessa esimerkiksi voiteluöljyjen ja biopolttoaineiden valmistuksessa. Työn tutkimus on tehty pintafysiikan tavanomaisilla menetelmillä, kuten röntgenfotoelektroni-spektroskopialla, matalaenergisten elektronien diffraktiolla, tunnelointimikroskopialla ja termisellä desorptiospektroskopialla. Lisäksi työssä esitellään yhteistyökumppanien muilla kokeellisilla sekä laskennallisilla menetelmillä saavuttamia tuloksia.

Fosforin adsorption kummallekin yksittäiskidepinnalle havaittiin olevan tehokkaampaa, mikäli pinnan lämpötilaa nostetaan. Pinnan toivutus fosforin annostelun jälkeen tuotti järjestyneitä rakenteita. Näitä löydettiin useampia erilaisia erisuuruisilla fosforipeitoilla. Kyllin suurilla annoksilla peitto saturoitui kummallakin pinnalla. Fosforin havaittiin myös muodostavan moniatomisia klustereita. Hapetuskatalyyttipinnoilla fosfori muodosti fosfaattiyhdisteitä katalyyttien tukiaineiden kanssa. Se aiheutti myös morfologisia muutoksia: esimerkiksi katalyyttipinnan alan huomattiin pienenevän. Katalyyttisen aktiivisuuden väheneminen vaihteli kohtalaisesta merkittävään eri katalyyttien ja hapetusreaktioiden välillä. Rikin puolestaan huomattiin lieventävän fosforimyrkytystä. Maleiinianhydridi muodosti järjestymättömiä usean kerroksen rakenteita platina (111) -pinnalle. Molekyylit desorboituivat pinnalta tai hajosivat jo alle huoneenlämmössä. Hajonneiden molekyylien osien desorptiota havaittiin tätä korkeammissa lämpötiloissa. Työssä saavutetut tulokset tuovat omalta osaltaan lisätietoa fosforin aiheuttamasta katalyyttimyrkytyksestä. Toisaalta tulokset ovat myös osa pintatieteen perustutkimuksen jatkumoa.

Preface

This doctoral thesis is the end result of a five years' work, or at least a concrete manifestation thereof. Although this book itself has been written by me, the work behind has been carried out by numerous people, to whom I would now like to express my deepest gratitude.

First and foremost, I would like to thank my instructor and group leader Dr. Jouko Lahtinen. Without him, this piece of work would never have materialized. To begin with, Jouko gave me the opportunity to start working towards the doctoral degree. He has given me freedom to carry out my research independently, but he has also been there to answer any question or take a wrench into his own hand whenever necessary. Being the first person to turn to, Jouko has taught me a really great deal about surface science and especially our equipment.

Many current and past members of our group and the department have had a huge impact on my research. I am extremely grateful to Dr. Jani Sainio for always having time for my problems and for being crucial to gaining, interpreting and presenting many main results in this work. I want to thank Dr. Sampsa Hämäläinen for patiently teaching me how to use our equipment and for helping me out many times. Prof. Peter Liljeroth deserves my gratitude for his ever-supportive attitude and the constructive feedback that improved the thesis. I am grateful to Dr. Godhuli Sinha and Lic. Sc. Ville Viitanen from whom I learnt a lot at the beginning of my doctoral studies. I would also like to thank Dr. Klaus Rytsölä for the many times he has helped us out with our measurement electronics.

Much of the work reported here has been carried out together with other research groups. I would like to thank our collaborators at University of Oulu, Tampere University of Technology and Dinex Ecocat, especially Dr. Mari Honkanen, M. Sc. Marja Kärkkäinen and Dr. Ari Väliheikki. I want

also to express my gratitude to Prof. Adam Foster and Dr. Hugo Pinto for their co-operation. During my time as a doctoral candidate, I also had the privilege to instruct research assistants, and I would like to thank Ms. Minna Kauppila, Ms. Maaria Salmi, Mr. Toni Mäkelä and Mr. Ari Riihimäki for carrying out much of the laboratory work and for helping me to improve my skills as an instructor.

The majority of my work was funded by Academy of Finland through the ACaBio project. This is greatly appreciated. In addition, I am truly grateful to Jouko for securing the funding for the remainder of my studies.

I have been lucky to have many friends working for their doctoral theses at the same time. Their peer support has definitely been priceless. But fortunately, there is more to life than just work, and freetime activities have brought some refreshing variety into these years. In particular, I would like to thank the members of Fyysikkospeksi for all the good times and the people at InnoLok Ltd. for all the applications and abbreviations.

Lastly, I would like to thank my family. I am grateful to my parents Seija and Raimo for their ever-present mental and material support and encouragement. I thank my dear wife Tanja for everything possible, including but definitely not limited to sharing the everyday life with me and taking care of our home while I was finishing my thesis. And finally, I want to thank our son Leevi. He will not understand what that means yet, but there is a chance he may find the book itself tasty.

Espoo, March 17, 2017,

Olli Heikkinen

"For, we must never forget that if there was not one thing that was not on top of another thing, our society would be nothing more than a meaningless body of men that had gathered together for no good purpose."
    – The President of the Royal Society for Putting Things on Top of Other Things, 1970

Contents

List of Publications

This thesis consists of an overview and of the following publications which are referred to in the text by their Roman numerals.

I Godhuli Sinha, Olli Heikkinen, Matias Vestberg, Lotta Mether, Kai Nordlund and Jouko Lahtinen. Adsorption of maleic anhydride on Pt(111). *Surface Science*, 620, 9-16, February 2014.

II Olli Heikkinen, Hugo Pinto, Godhuli Sinha, Sampsa K. Hämäläinen, Jani Sainio, Sven Öberg, Patrick R. Briddon, Adam S. Foster and Jouko Lahtinen. Characterization of a Hexagonal Phosphorus Adlayer on Platinum (111). *Journal of Physical Chemistry C*, 119, 12291-12297, May 2015.

III Olli Heikkinen, Ari Riihimäki, Jani Sainio and Jouko Lahtinen. Phosphorus adlayers on platinum (110). *Surface Science*, 17 pages, submitted in January 2017.

IV Marja Kärkkäinen, Tanja Kolli, Mari Honkanen, Olli Heikkinen, Mika Huuhtanen, Kauko Kallinen, Toivo Lepistö, Jouko Lahtinen, Minnamari Vippola and Riitta L. Keiski. The Effect of Phosphorus Exposure on Diesel Oxidation Catalysts—Part I: Activity Measurements, Elementary and Surface Analyses. *Topics in Catalysis*, 58, 961-970, October 2015.

V Mari Honkanen, Marja Kärkkäinen, Olli Heikkinen, Kauko Kallinen, Tanja Kolli, Mika Huuhtanen, Jouko Lahtinen, Riitta L. Keiski, Toivo

Lepistö and Minnamari Vippola. The Effect of Phosphorus Exposure on Diesel Oxidation Catalysts—Part II: Characterization of Structural Changes by Transmission Electron Microscopy. *Topics in Catalysis*, 58, 971-976, October 2015.

VI Marja Kärkkäinen, Tanja Kolli, Mari Honkanen, Olli Heikkinen, Ari Väliheikki, Mika Huuhtanen, Kauko Kallinen, Jouko Lahtinen, Minnamari Vippola and Riitta L. Keiski. The Influence of Phosphorus Exposure on a Natural-Gas-Oxidation Catalyst. *Topics in Catalysis*, 59, 1044-1048, July 2016.

VII Ari Väliheikki, Tanja Kolli, Mari Honkanen, Olli Heikkinen, Marja Kärkkäinen, Kauko Kallinen, Mika Huuhtanen, Minnamari Vippola, Jouko Lahtinen and Riitta L. Keiski. The Impact of Sulphur, Phosphorus and their Co-effect on Pt/SiO_2-ZrO_2 Diesel Oxidation Catalysts. Accepted for publication in *Topics in Catalysis*, 5 pages, May 2016.

Author's Contribution

Publication I: "Adsorption of maleic anhydride on Pt(111)"

The author performed the measurements and their analysis together with the first author and participated in writing the manuscript.

Publication II: "Characterization of a Hexagonal Phosphorus Adlayer on Platinum (111)"

The author performed most of the measurements and analysis and wrote the manuscript excluding the computational sections.

Publication III: "Phosphorus adlayers on platinum (110)"

The author planned the work, performed the experiments and analysis together with the other authors and wrote the manuscript.

Publication IV: "The Effect of Phosphorus Exposure on Diesel Oxidation Catalysts—Part I: Activity Measurements, Elementary and Surface Analyses"

The author was responsible for the XPS measurements and analysis and participated in discussions and interpretation of all the results.

Publication V: "The Effect of Phosphorus Exposure on Diesel Oxidation Catalysts—Part II: Characterization of Structural Changes by Transmission Electron Microscopy"

The author was responsible for the XPS measurements and analysis and participated in discussions and interpretation of all the results.

Publication VI: "The Influence of Phosphorus Exposure on a Natural-Gas-Oxidation Catalyst"

The author was responsible for the XPS measurements and analysis, wrote the respective parts of the manuscript and participated in discussions and interpretation of all the results.

Publication VII: "The Impact of Sulphur, Phosphorus and their Co-effect on Pt/SiO$_2$-ZrO$_2$ Diesel Oxidation Catalysts"

The author was responsible for the XPS measurements and analysis, wrote the respective parts of the manuscript and participated in discussions and interpretation of all the results.

1. Introduction

Surface science is a branch of physics, chemistry and material science studying phenomena taking place in the vicinity of the outermost atomic layers of solid material, i.e. surfaces. Although some related studies were carried out much earlier, the field of research was really commenced only in the 1960s, utilizing the newly developed vacuum technology and analytical techniques as well as advancements in computer technology. A prominent segment of surface science are studies of geometrically well-defined crystalline surfaces, single crystals in particular, and reactions between them and surrounding molecules in gas phase.

Adsorption is one of the most studied phenomena in surface science. It means bond formation between surface atoms and a particle condensing from vapour phase. A weak adsorption through van der Waals bonds is called physisorption, whereas a stronger sticking through ionic or covalent bonds is known as chemisorption. A chemisorbed adsorbate alters its chemical state and may also dissociate in order to form more efficiently binding adsorbate species. Chemisorption may also have a strong effect on the substrate surface, from slightly dislocating the surface atoms to causing a complete reconstruction on the topmost atomic layers. In general, adsorption kinetics are expressed as

$$\frac{\mathrm{d}\Theta}{\mathrm{d}t} = s_0 I f(\Theta) \exp\left(-\frac{E_{\mathrm{act}}}{k_{\mathrm{B}}T}\right), \tag{1.1}$$

where Θ is the coverage of the adsorbate, s_0 its initial sticking coefficient and I the flux of impinging adsorbate particles. If the adsorption reaction requires thermal activation (E_{act}) its effect is expressed in the exponential part. $f(\Theta)$ is the probability function for an adsorbate particle to find an available adsorption site, and there are several models and definitions of varying complexity for it, the simplest being $f(\Theta) = 1 - \Theta$. In many cases, adsorption is precursor-mediated, meaning that adsorbates are first bonded weakly, finding then the final adsorption sites, possibly through

dissociation, recombination and diffusion. Figure 1.1 illustrates potential energy landscape in two simple example cases of adsorption. [1]
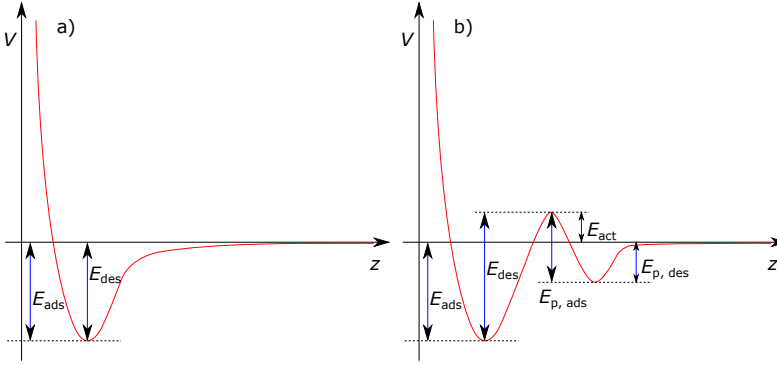
Figure 1.1. Schematic potential energy curves (red) as a function of adsorbate-surface distance in two example cases of adsorption. (a) Simple non-activated chemisorption. (b) Activated precursor-mediated chemisorption. The gas-phase particle is first physisorbed weakly on the surface. The activation energy barrier E_{act} must be overcome for the stronger chemisorption to take place. E_{ads} is the binding energy for a chemisorbed particle and E_{des} the energy barrier for desorption. $E_{\mathrm{p,ads}}$ and $E_{\mathrm{p,des}}$ mean the energy barriers for chemisorption and desorption from the precursor state.

Desorption means the process of an adsorbate particle leaving the surface. This requires energy which can be gained for instance from thermal vibrations of the surface atoms. Therefore, elevating the substrate temperature may give rise to desorption. A simplified model for desorption is given by Polanyi-Wigner equation, bearing resemblance to equation 1.1, written as

$$-\frac{\mathrm{d}\Theta}{\mathrm{d}t} = k_n \Theta^n \exp\left(-\frac{E_{\mathrm{des}}}{k_{\mathrm{B}}T}\right), \qquad (1.2)$$

where k_n is a constant and n the kinetic order. The simplest case $n = 1$ refers to a system where adsorbates desorb independently of each other, and remain intact in the process. [1]

A research topic in surface science with major practical importance is catalysis. Catalysis means enhancement of chemical reactions by offering the reactants an alternate pathway, thus decreasing the activation energy needed for the reaction to start and increasing the reaction rate. Catalysis requires a catalyst, a substance that reacts with the actual reactants to form intermediates but is not consumed in the overall reaction. Catalysis is applied in an enormous number of industry-scale chemical processes. Since catalytic reactions are versatile, so is the range of catalysts [2]. In oxidation and reduction reactions, for instance, transition metals are efficient. Platinum in particular has been widely both studied and used in

technological applications [3, 4]. Since catalytic reactions happen on surfaces, utilizing adsorption and desorption, the surface area needs to be as large as possible in practical applications. Therefore, the catalyst is often dispersed on a surface of a porous support material [5, 6].

Catalytic converters for automotive exhaust gases are an important application of catalysis. Ideally, combustion of fuels produces only water and carbon dioxide, but in practice, exhaust gases contain also carbon monoxide, hydrocarbons (HC) and nitrogen oxides (NO_x), for instance [7]. To reduce their emission, modern cars are equipped with catalytic converters. The main oxidation reactions in exhaust gas catalysis are [7]

$$C_mH_n + \left(m + \frac{n}{4}\right)O_2 \rightarrow mCO_2 + \frac{n}{2}H_2O, \tag{1.3}$$

$$CO + \frac{1}{2}O_2 \rightarrow CO_2, \tag{1.4}$$

$$CO + H_2O \rightarrow CO_2 + H_2. \tag{1.5}$$
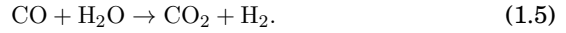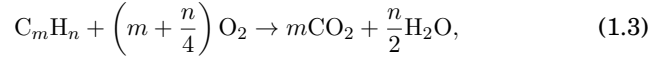
Thus, catalytic conversion aims at decreasing CO and HC emissions, simultaneously increasing production of CO_2 which itself is a greenhouse gas, yet less harmful [8]. The oxidation reaction of methane (CH_4), a special case of equation 1.3, is relevant in natural gas combustion applications [9–11]. Nitrogen oxides are being reduced according to reactions [7]

$$NO + CO \rightarrow \frac{1}{2}N_2 + CO_2, \tag{1.6}$$

$$NO + H_2 \rightarrow \frac{1}{2}N_2 + H_2O. \tag{1.7}$$
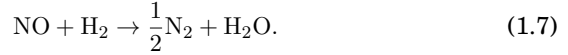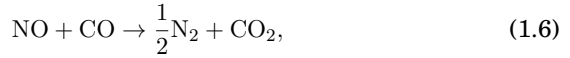
Equations 1.6 and 1.7 are valid also for higher oxidation states with different stoichiometric ratios. Furthermore, some catalysts also oxidise NO due to more efficient reduction of NO_2 [12, 13]. In addition to CO, HC and NO_x, exhaust gases may also contain SO_2, large carcinogenic molecules and solid particulate matter [14, 15].

Catalytic deactivation means a reduced efficiency of a catalyst to take part in the reactions it should. The reasons behind deactivation are either physical or chemical. The main mechanism of the former is sintering, meaning particle size growth due to migration. If a catalyst has a temperature high enough for heat to overcome the activation energy of migration, catalyst atoms or larger crystals diffuse on the surface, colliding and binding with each other, forming larger clusters. This decreases the surface area and the number of adsorption sites, thus decreasing also the activity. Chemical deactivation, or poisoning, means chemisorption of unwanted particles on the catalyst surface. They either block the active

sites, or alter the chemical or electronic environment of the catalyst. The poisoning effect may be reversible or permanent, and the poison particles may adsorb selectively, preferring some adsorption sites over others, or uniformly. Figure 1.2 illustrates the two main types of catalyst deactivation. [16–18]
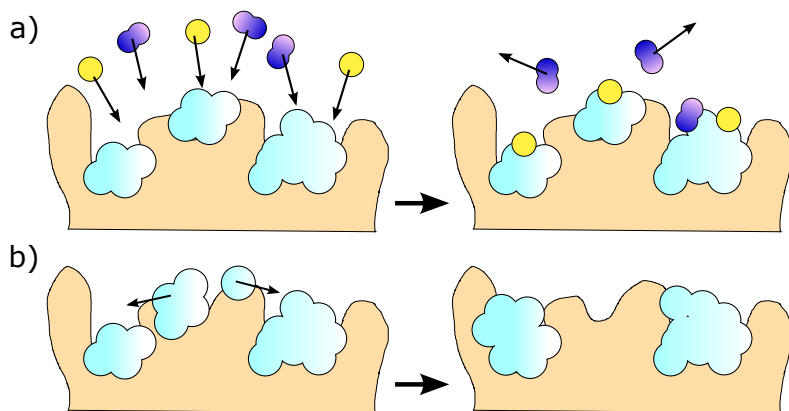
Figure 1.2. Two main types of catalyst deactivation. (a) Catalyst poisoning occurs, when unwanted particles (yellow) adsorb on the active sites (light blue) on a catalyst surfaces, blocking the sites or altering the surface chemistry so that adsorption of other particles (purple) is prevented. (b) Sintering occurs, when thermally activated catalyst particles migrate and form larger clusters, thus decreasing the active surface area.

There are several poisons typical to automotive exhaust gas catalysis. Before the introduction of lead-free fuels, catalytic converters did not become common due to the strong poisoning effect of lead, especially towards palladium [19]. Sulfur is a catalyst poison, traces of which can be found in fuels as a part of different organic compounds. During combustion it generally oxidizes to SO_2, and possible further to SO_3 or a sulfate compound (SO_4^{2-}). The deactivation effect caused by SO_2 is the strongest of these although H_2S causes even stronger effect. Palladium may form palladium sulfate, but platinum is generally more resistant to sulfur, as are support materials SiO_2 and ZrO_2. [16–18, 20]

Phosphorus is a strong catalyst poison causing an irreversible effect and originating from lubricants and oil additives. It often appears as a part of phosphate compounds (PO_4^{3-}). It can react with other elements found in additives, as well as particles in the catalyst support. Phosphorus poisoning has been diminished with competing poisons calcium and barium, but decreasing phosphorus in oil additives has appeared to be the most efficient way to avoid the poisoning effect. [16, 21]

To gain more insight into catalyst poisoning, adsorption of poisons on single crystals has been studied quite widely. In this way, the fundamental reactions between the two elements, poison and catalyst, can be examined. Moreover, single crystal microfacets are present in real industry-scale catalysts as well [22]. For instance, adsorption of sulfur on single crystal surfaces of transition metals and its effect of CO adsorption have been covered quite extensively in literature [23–30]. Phosphorus, on the other hand, has received less attention. Adsorption and dissociation of phosphine (PH_3) has been studied on various transition metal surfaces [31–34], and phosphate adsorption on platinum surfaces [35–37] has been examined. On semiconductor single crystals, especially silicon, adsorption studies of phosphorus have been carried out in larger numbers [38–43].

In this work, adsorption of phosphorus and its poisoning effect has been studied both with single crystal platinum surfaces, as well as real platinum and platinum-palladium catalysts for automotive applications. These phenomena are studied with typical techniques of surface science, such as X-ray photoelectron spectroscopy, low-energy electron diffraction and scanning tunnelling microscopy, presented in more detail in Chapter 2. The automotive catalyst studies have been carried out in collaboration with research groups in University of Oulu and Tampere University of Technology, the author of this work being responsible for the chemical analysis with X-ray photoelectron spectroscopy. The studied catalyst samples have been natural gas oxidation (NGO) [9, 10, 44] and diesel oxidation catalysts (DOC) [13, 45] for lean-burn engines. Chapter 3 reviews the results of the publications, while Chapter 4 summarizes the work.

Distinct from the rest of this work, Publication I concentrates on maleic anhydride adsorption on platinum (111). Maleic anhydride ($C_4H_2O_3$) is a cyclic, organic molecule used as an intermediate in manufacturing processes of e.g. pharmaceuticals, polyester resins and oil additives. Due to its importance in industry, studying its reactions with a well-established catalyst such as platinum is an interesting topic. While the study is not directly connected to phosphorus or catalyst poisoning, it is however related to the wider topics of catalysis and exhaust gas emission control. Like phosphorus, maleic anhydride is also used in production of oil additives for combustion engines. Moreover, it is an example of oxygenated carbon-ring molecules which have potential in processes transferring biomass into fuels. [46–48].

2. Experimental Methods

2.1 X-ray photoelectron spectroscopy

X-ray photoelectron spectroscopy (XPS) is a non-destructive and surface sensitive technique for chemical characterization, based on photoelectric effect and detection of escaping electrons. XPS is customarily used for determining both relative concentrations of chemical elements and the chemical environment of each element. XPS data is vastly reported in literature and its availability is highly utilized in XPS analysis.

The photoelectic effect means electron emission from an atom after photon absorption. It can be written as

$$h\nu = W + K_{\max},$$ (2.1)

where photon energy $h\nu$ is consumed by the work W required for dislocating an electron from its shell and then transferred into the kinetic energy $K_{\max}$ of the escaping electron, often called a photoelecton. Binding energy E_b can be defined as the energy difference between a bound electron state and Fermi energy. This enables rewriting equation 2.1 as

$$E_b = h\nu - K_{\max} - \phi.$$ (2.2)

Here, ϕ is an analyzer-dependent workfunction, a correction factor for small energy shifts induced by the instrument. It is generally known for a given set-up [49]. In an XPS measurement, the photoelectric effect is triggered with photons of known energy $h\nu$, and the observable being measured is the kinetic energy of photoelectrons. Thus, the right-hand side of equation 2.2 is completely known, solving also the binding energy of each incoming photoelectron. The initial result of an XPS measurement is a spectrum showing photoelectron intensities as a function

of their binding energies (figure 2.1a). Each chemical element gives rise to a characteristic set of photoelectron lines, due to photoelectrons originating from different orbitals and spin-orbit coupled states. The elements on the measured sample surface can then be identified by comparing the detected lines to those in literature.

As figure 2.1a shows, XPS spectra tend to have non-idealities. The photoelectron lines have a non-zero width caused by photon energy variations, analyzer properties and the non-zero lifetime of an empty core state of an ion [49]. The rising background is due to photoelectrons originating from atoms below the surface. They experience inelastic collisions before escaping the solid sample, having thus low kinetic energy when reaching the analyzer and appearing at correspondingly higher binding energy values in the spectra. Therefore, equation 2.2 only works when $K = K_{\max}$. In addition, an XPS spectra may show additional peaks due to photons with different characteristic energy, Auger process (see Section 2.2) and shake-up effects, for instance.
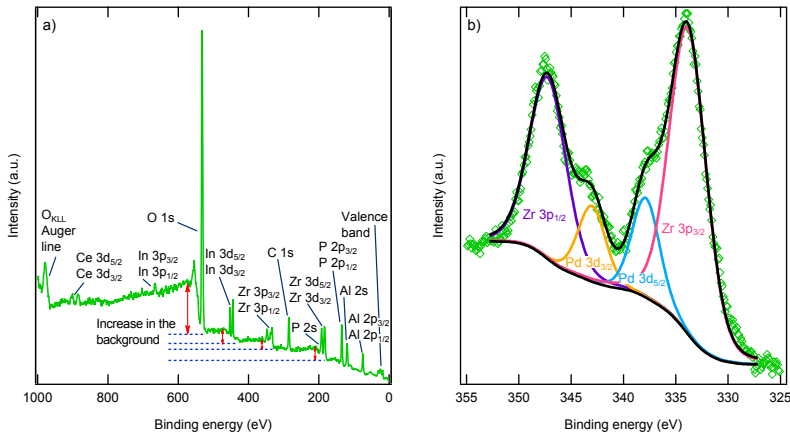
Figure 2.1. (a) An X-ray photoelectron spectrum of a Pt-Pd catalyst. In addition to the photoelectron lines, the spectrum features an Auger line and notable increase in the inelastic background. (b) A higher-resolution scan of a 30 eV wide region shows photoelectron lines of Zr 3p and Pd 3d orbitals. Iterative Shirley background subtraction and Lorentzian-Gaussian peak fitting have been applied to deconvolute the four lines.

The photoelectron line intensity given by an arbitrary element A on a surface is

$$I_{A,0} = k\sigma_A C_A, \tag{2.3}$$

where σ_A is a photoemission cross section expressing the probability for the particular photon to cause an emission of an electron in the particular shell, and C_A is the atomic concentration of element A, as atoms per unit

volume [50]. k incorporates factors coming from electronics, geometry and optics and can be considered an energy-dependent constant for a given set-up. When the photoemission takes place below the topmost atomic layer, the photoelectron line intensity is attenuated exponentially, and at a depth of t it can be written as [51]

$$I_{\text{A},t} = I_{\text{A},0}\exp\left(\frac{-t}{\lambda_\text{A}\cos\theta}\right), \tag{2.4}$$

Here, λ_A is the inelastic mean free path (IMFP) of a given photoelectron, meaning the average length the electron can travel in the solid sample without inelastic collisions [52], and θ is the angle between the sample surface normal and the analyzer entrance. The exponential attenuation gives XPS its surface sensitive nature with information depth of 5 to 15 nm [49]. The total intensity of a photoelectron line is the integral of $I_{\text{A},t}$ over the whole sample thickness. If the sample is homogenous for the total information depth, the sample can be treated as semi-infinite, giving

$$I_\text{A} = k\sigma_\text{A}C_\text{A}\int_0^\infty \exp\left(\frac{-z}{\lambda_\text{A}\cos\theta}\right)\mathrm{d}z = k\sigma_\text{A}C_\text{A}\lambda_\text{A}\cos\theta. \tag{2.5}$$

Usually, there is no need to determine absolute atomic densities C_A, but relative concentrations c_A instead. With the help of equation 2.5, they can be written

$$c_\text{A} = \frac{C_\text{A}}{\sum_i C_i} = \frac{I_\text{A}\sigma_\text{A}^{-1}\lambda_\text{A}^{-1}}{\sum_i I_i\sigma_i^{-1}\lambda_i^{-1}}. \tag{2.6}$$

Thus, atomic percentages can be calculated by measuring intensities and knowing IMFP's and photoemission cross sections. The IMFP's are usually approximated as a rising function of K, in this work as

$$\lambda = \left(\frac{h\nu - E_b}{h\nu - E_{\text{C1s}}}\right)^{0.7}. \tag{2.7}$$

The photoemission cross sections, also known as Scofield factors, are widely available in data libraries [53]. E_{C1s} is the binding energy of adventitious carbon [54].

The intensity given by equation 2.5 can be applied when estimating a finite thickness t or coverage percentage f of an adlayer. The ratio between the intensities of adsorbate and substrate materials can be written

$$\frac{I_\text{a}}{I_\text{s}} = \frac{f\sigma_\text{a}\lambda_\text{a}[1 - \exp(-\frac{t}{\lambda_\text{a}\cos\theta})]}{f\sigma_\text{s}\lambda_\text{s}\exp(-\frac{t}{\lambda_{\text{a,s}}\cos\theta}) + (1-f)\sigma_\text{s}\lambda_\text{s}}. \tag{2.8}$$

λ_a and λ_s represent effective attenuation lengths of electrons originating from the adsorbate and the substrate, respectively, while $\lambda_{\text{a,s}}$ refers to the substrate electrons attenuated by an adsorbate layer.

Different chemical environments give rise to binding energy shifts of XPS lines. These shifts take into account the change in valence charge, atom-atom interactions, and a relaxation after a photoemission [50]. A rule of thumb states that bonding with electronegative atoms increases E_b [49]. The shifts corresponding to different molecules and moieties are well-tabulated.

Due to the non-idealities in XPS spectra, evaluating line intensities requires eliminating the inelastic background and taking the broadening of the peaks into account. In this work, the contribution of the background is estimated with Shirley background subtraction, a regularly used empirical technique [55]. The Shirley function $F_k(E)$ for an XPS spectrum $j(E)$ is defined iteratively

$$F_k(E) = j(E) - j(E_{\min}) \frac{\int_E^{E_{\max}} F_{k-1}(T)\mathrm{d}T}{\int_{E_{\min}}^{E_{\max}} F_{k-1}(T)\mathrm{d}T}. \tag{2.9}$$

Because of the non-zero line widths, I_A in equation 2.5 must be regarded as the area of the peak. It can be calculated as a point-by-point integral, or by fitting a theoretical curve to the data. Since the phenomena behind the binding energy deviation are Lorentzian and Gaussian by nature [49, 56], a convoluted curve of

$$L(E) = \left[1 + \left(\frac{E_b - E}{\beta} \right)^2 \right]^{-1} \tag{2.10}$$

and

$$G(E) = \exp \left[-\ln 2 \left(\frac{E_b - E}{\beta} \right)^2 \right] \tag{2.11}$$

is needed for a physically correct fit. β is half width at half maximum. The fitting itself means iterative chi-square minimisation [57, 58]. Figure 2.1b shows an example of background subtraction and peak fitting applied to a spectrum.

A schematic of XPS is shown in figure 2.2. An X-ray gun is operated with a high-voltage source, and it produces a characteristic X-ray beam, in this work either Al or Mg K_α. If a monochromator is applied, it filters out unwanted photon frequencies before the beam hits the sample. The photoelectrons are collected in the electron energy analyzer with a set of electric lenses. The analyzer produces an electric field guiding only photoelectrons with a given kinetic energy into the detector which counts the incoming electron impulses. By applying gradually different voltages in the analyzer, a whole spectrum of kinetic energies can be measured. The detector signal is then electrically amplified and converted into the XPS spectrum.
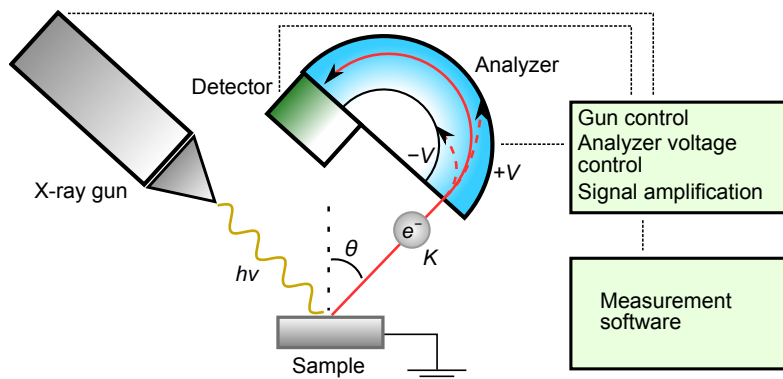
Figure 2.2. A simplified illustration of an XPS set-up features an X-ray gun, a hemispherical analyzer and a detector. Their operation is controlled by control units and measurement software.

2.2 Auger electron spectroscopy

Auger electron spectroscopy (AES) is a technique for chemical characterization. It is conceptually similar to XPS but based on a different phenomenon. The Auger emission process is illustrated in figure 2.3. First, an incident electron (or X-ray photon) collides with an atom, giving an electron enough energy to be emitted. To de-excite the ion, another electron from a higher orbital fills the empty state. The energy freed in this process is acquired by a third electron, or an Auger electron, which will be emitted, making the initial atom doubly ionized. The kinetic energy of an Auger electron after an arbitrary transition is approximately given by the binding energies of the electrons involved as

$$K_{abc} = E_a - E_b - E_c - \phi, \tag{2.12}$$

where a, b and c refer to arbitrary orbitals, and ϕ is the workfunction of the system. However, this simplest possible form does not take shifts caused by ionization and core holes into account [49,59]. There are multiple possible transitions, and their amount increases with atomic number.

An AES spectrum shows the Auger electron count as a function of their kinetic energy ($N(K)$ vs. K). Each chemical element produces a characteristic set of peaks. As with XPS, these are readily available in data libraries. In addition to the Auger electron peaks a typical AES spectrum shows a continuous background caused by inelastically backscattering electrons. To distinguish the peaks clearly from the background, the spectra are usually shown in differentiated form ($\frac{\mathrm{d}N(K)}{\mathrm{d}K}$ vs. K) which is

11
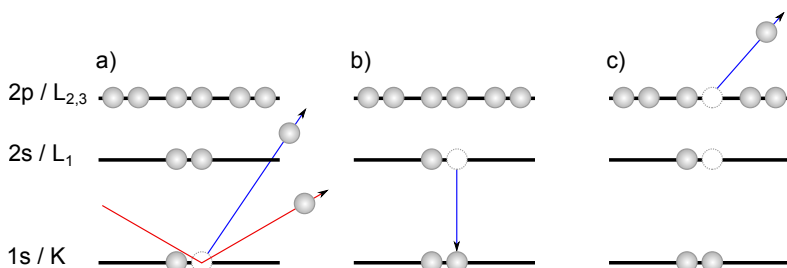
Figure 2.3. A $KL_1L_{2,3}$ Auger process involves (a) electron emission from the core level due to an incoming electron or photon, (b) a $L_1 \rightarrow K$ transition and (c) a $L_{2,3}$ electron emission.

achieved by using the measurement software or the electronics. See figure 2.4 for an example. To determine atomic percentages, expressions similar to XPS can be derived. Chemical compounds can be identified using energy shifts and changes in the peak form. However, in this work the role of AES was restricted to estimating adsorbate coverages when XPS was not available.
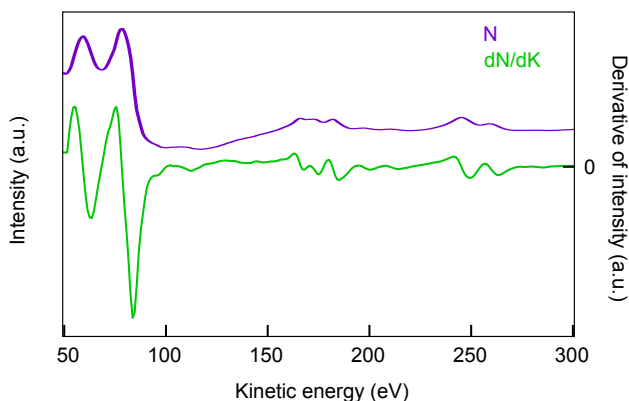
Figure 2.4. An Auger spectrum of a platinum (110) surface. Typically to AES, the initial spectrum has broad peaks and a relatively weak peak-to-background ratio, whereas the differentiated spectrum shows the peaks much more prominently.

The experimental set-up consists of an electron source, an analyzer and a detector combined with electronics (figure 2.5). In this work, a double-pass cylindrical mirror analyzer (DPCMA) has been employed. The electron source is a LaB_6 filament with initial electron energy of 10 keV [59]. It is located in the middle of the analyzer module, and the electron beam targets directly towards the sample. The Auger electrons reach the analyzer and with a given kinetic energy travel into the detector, not unlike to XPS.
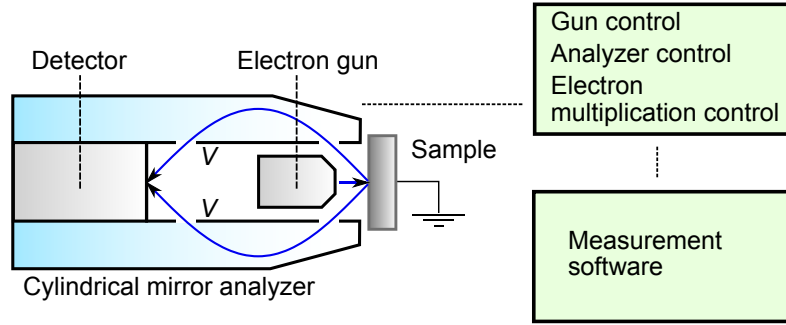
Figure 2.5. A highly simplified set-up for AES. The emitted Auger electrons travel through the cylindrical mirror analyzer. Due to the analyzer voltage, only electrons with certain kinetic energies can reach the detector, and changing the voltage produces a spectrum. The instruments are operated with rack-mounted controllers and measurement software.

2.3 Low-energy electron diffraction

Low-energy electron diffraction (LEED) is an indirect experimental method for structural characterization of surface lattices. It is based on the wave-like nature of electrons. The electrons are bombarded towards a sample surface and make an observable diffraction pattern on a fluorescent screen after back-scattering. The technique is well-suited for determining adlayers on single crystal surfaces. [60]

In one dimension, Bragg's law

$$d\sin\theta = n\lambda \tag{2.13}$$

expresses the angles in which two electrons diffracting from the topmost atomic layer interfere constructively. As figure 2.6a shows, this is equal to the condition where the path difference of two adjacent electrons is multiple of the wavelength of the electron. As electrons are particles, the wavelength here is de Broglie wavelength, which can be written as

$$\lambda = \frac{h}{\sqrt{2mK}}, \tag{2.14}$$

where h is Planck's constant, m the mass of an electron and K its kinetic energy. The inter-atomic distances in a metal lattice are in the magnitude of ångströms. In LEED, the incoming electrons usually have a kinetic energy between 20 and 500 eV. As equation 2.14 shows, their wavelength is in the same range with lattice constants. Since electrons with such a low energy have a short inelastic mean free path, only the electrons scattering from the topmost layers contribute. This makes LEED a highly surface

sensitive technique. Because of this, the single scattering approximation presented in figure 2.6a, is valid for initial LEED analysis.
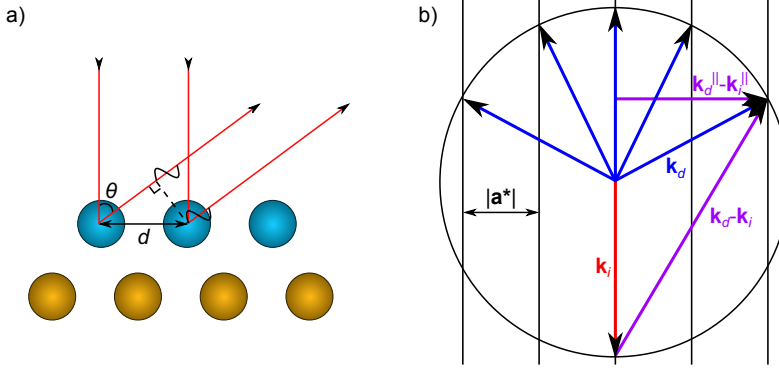
Figure 2.6. (a) Bragg's law in one dimension shows the relation between constructive interference, lattice constant and scattering angle. (b) Diffraction is often illustrated with Ewald's sphere construction. The parallel component of the difference between diffracted and incoming wave vectors gives the index of a diffraction spot.

Bragg's law can be generalized with Laue's equations. On a two-dimensional lattice with basis $(\mathbf{a}, \mathbf{b})$, the Laue conditions equivalent to Bragg's law are

$$\mathbf{a} \cdot (\mathbf{k}_d^{||} - \mathbf{k}_i^{||}) = 2\pi h \tag{2.15}$$

and

$$\mathbf{b} \cdot (\mathbf{k}_d^{||} - \mathbf{k}_i^{||}) = 2\pi k. \tag{2.16}$$

Above, $\mathbf{k}_i^{||}$ and $\mathbf{k}_d^{||}$ are the components of wave vectors parallel to surface for the incident and diffracted electron waves, respectively, and h and k are the Miller indices for the reciprocal lattice vector

$$\mathbf{G} = h\mathbf{a}^* + k\mathbf{b}^*, \tag{2.17}$$

where the basis $(\mathbf{a}^*, \mathbf{b}^*)$ for the reciprocal lattice is defined as

$$\mathbf{a}^* = 2\pi \frac{\mathbf{b} \times \mathbf{n}}{|\mathbf{a} \times \mathbf{b}|} \tag{2.18}$$

and

$$\mathbf{b}^* = 2\pi \frac{\mathbf{n} \times \mathbf{a}}{|\mathbf{a} \times \mathbf{b}|}. \tag{2.19}$$

Here, $\mathbf{n}$ is the unit normal vector of the 2D lattice. The equations 2.15 to 2.19 imply that

$$\mathbf{G} \cdot (\mathbf{a} + \mathbf{b}) = 2\pi(h + k) = (\mathbf{a} + \mathbf{b}) \cdot (\mathbf{k}_d^{||} - \mathbf{k}_i^{||}), \tag{2.20}$$

and thus

$$\mathbf{G} = \mathbf{k}_d^{||} - \mathbf{k}_i^{||}. \tag{2.21}$$

Furthermore, when the electron beam is perpendicular to the sample surface, as often is the case in a LEED set-up, the component $\mathbf{k}_i^{||}$ becomes zero. Therefore,

$$\mathbf{G} = \mathbf{k}_d^{||}, \qquad (2.22)$$

which essentially means that the diffraction pattern given by LEED expresses the reciprocal lattice of the sample surface. A conventional geometric interpretation for this is the Ewald's sphere, shown in figure 2.6b. [1]

Using the reciprocal lattice, the real lattice can be deduced. The usefulness of LEED is often due to the adsorption structures having a larger unit cell than the substrate. This gives rise to extra diffraction spots, and their mutual distance compared to the spots caused by the substrate unit cell will reveal the adsorbate symmetry. In practice, this is not always trivial, as figure 2.7 illustrates. LEED patterns may have multiple domains, which especially complicates the analysis. The origin of the domains is that adsorbate structures may have several equivalent directions of growth based on rotational and reflectional symmetries of the substrate lattice. Even though the domains may be distinct, in the reciprocal lattice they overlap. Similarly, diffraction patterns of two completely different superstructures may overlap, which can further complicate determining the structures. On the other hand, a LEED pattern may be seen even if the sample surface is only partially ordered or in the presence of impurities. This is because the diameter of the incident electron beam is around one 1 mm while ordered areas of 20 nm × 20 nm are large enough to be detected.
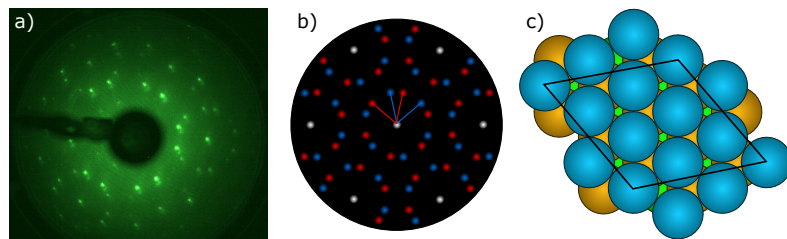
Figure 2.7. An example of interpretation of LEED data. (a) An actual diffraction pattern of CH_3S on Ag(111). (b) The pattern consists of two domains with mirroring symmetries (blue and red) and the diffraction spots of the substrate (white). (c) The corresponding unit cell in real space has a $\sqrt{7} \times \sqrt{7} - R19.1°$ symmetry.

A major drawback of LEED is that it only determines the symmetry of the superstructure, i.e. the size and shape of the adsorbate lattice unit cell. It directly gives no information of the structure or adsorption sites

within this unit cell, the LEED pattern being the same whether it encloses one atom or a complicated set of compounds. In order to solve the complete atomic level structure, LEED-$I(V)$ analysis can be applied. This requires taking more scattering effects than those at the topmost layer into account, leading to destructive interferences making each diffraction spot disappear at some energies. In practice, the $I(V)$ analysis is carried out by calculating peak intensities as a function of incident electron energy, and performing diffraction simulations for model systems, making changes to the model until the simulated $I(V)$ curves agree with the experimental ones. [61]
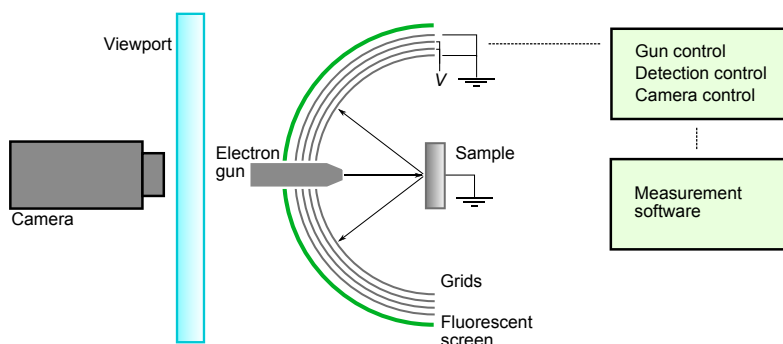
Figure 2.8. A reverse view LEED set-up consists of a small-sized electron gun in the middle of a hemispherical fluorescent screen collecting the electrons passing the electric grids. The pattern in the screen is recorded behind the gun.

Figure 2.8 shows a simplified LEED set-up. An electron gun points towards the sample in UHV conditions. The diffracted electrons enter a series of hemispherical electrical grids. They filter out inelastically scattered electrons. Finally, the electrons hit the fluorescent screen behind the grids. The impact with electrons gives rise to macroscopic luminescence effects, making the diffraction pattern, i.e. the reciprocal lattice directly visible. The instrument module is equipped with a viewport flange, and the information is collected with a camera directed towards the screen outside UHV.

2.4   Scanning tunnelling microscopy

Scanning tunnelling microscopy (STM) is a technique for direct imaging of surface structures. It is based on quantum mechanical tunnelling between the sample surface and a movable metal probe tip above it. STM is one variety of scanning probe microscopy (SPM) and one of the few ex-

perimental methods capable of achieving a sufficient resolution to observe individual atoms. [62, 63]

A simplified working principle of STM can be derived from elementary quantum mechanics. Namely, the gap between the tip and the sample can be regarded as a one-dimensional finite potential barrier as the red dashed line in figure 2.9a illustrates. The time-independent Schrödinger equation

$$-\frac{\hbar^2}{2m}\frac{\mathrm{d}^2}{\mathrm{d}x^2}\psi(x) + V(x)\psi(x) = E\psi(x), \tag{2.23}$$

where $\hbar$ is the reduced Planck constant and m is the mass of an electron, has two types of solutions in this potential. In the tip and the sample, the electrons behave like free particles, and the wave function becomes

$$\psi(x) = Ce^{\pm ikx}, \tag{2.24}$$

where C is the amplitude of wave function, depending on the direction of the electrons and whether they are in the tip or the sample. The plus sign denotes electrons propagating from left to right in figure 2.9a, and the minus sign vice versa. Furthermore,

$$k = \frac{\sqrt{2mE}}{\hbar}. \tag{2.25}$$

The potential energy V in equation 2.23 is E_{vac} in the barrier. If it is higher than the electron energy E, the wave function inside the barrier becomes

$$\psi(x) = De^{-\kappa x}, \tag{2.26}$$

where

$$\kappa = \frac{\sqrt{2m(E_{\mathrm{vac}} - E)}}{\hbar}. \tag{2.27}$$

Thus, the probability for an electron to propagate from the tip to the sample decays exponentially over the gap between them, but is nevertheless non-zero. This classically forbidden phenomenon is called quantum mechanical tunnelling.

If an electron in the tip faces the potential barrier, it either tunnels through it or is reflected back. Therefore, the transmission and reflection probabilities must sum up to unity. The transmission probability T is given by the absolute square of the amplitude (C in equation 2.24) of a transmitted wave function, and all the amplitudes are given by the boundary conditions of the wave functions. With this information, T can be solved analytically. For systems with a relatively high and wide potential barrier, an approximate solution

$$T \propto e^{-2\kappa L}, \tag{2.28}$$
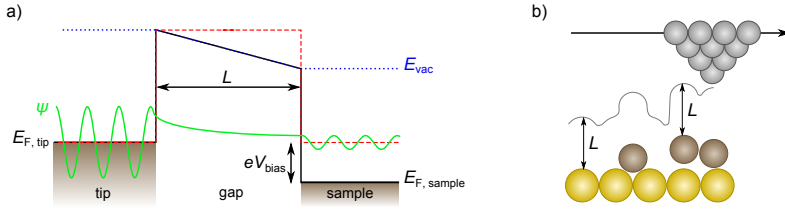
Figure 2.9. (a) A potential barrier serves as a simplified model for the tunnelling junction. Applying a voltage bias gives rise to a measurable net tunnelling current. (b) In a constant current scanning mode, the tip-sample distance is preserved throughout a measurement, and the tip height determines the sample surface topography.

where L is the gap width, can be derived. Since electric current essentially means the number of passing electrons per unit time, the tunnelling current I is directly proportional to the number of transmitted electrons and again to the transmission probability. Thus,

$$I = I_0 e^{-2\kappa L}, \tag{2.29}$$

where I_0 is constant.

When the gap width is small enough for tunnelling, the tip-vacuum-sample junction reaches equilibrium, and the Fermi levels of both the tip and the sample align. Then, tunnelling to either direction is equally probable, decresing the net electron flux and therefore also the tunnelling current to zero. In order to raise a tunnelling current, a bias voltage is applied to the sample (or the tip). This misaligns the Fermi levels as illustrated with the black solid line in figure 2.9a. Due to the misalignment, there are available empty states only in the sample for electrons in the tip to tunnel to (or vice versa, depending on how the biasing is chosen) and thus the current flows as defined in equation 2.29. This is used to conduct an STM measurement in the following way. While the sample is scanned laterally, the current is recorded by a feedback circuit which controls the tip movement in z direction. The z coordinate of the tip is changed so that the tunnelling current remains constant. The z axis movement is recorded for each (x, y) point, and lateral raster scanning reveals the topography of the scanned area. This measurement mode, illustrated in figure 2.9b, is called the constant current mode. Alternatively, constant height mode, where the z coordinate is not altered but the changes in the current are recorded, may be applied as well. Equations 2.27 and 2.29 give natural limitations of scale for STM. Since the work function $E_{\mathrm{vac}} - E$ is usually a couple of electron volts, the tunnelling current may

decay one order of magnitude when the barrier width is increased by an ångström [1]. Therefore, STM requires the tip-sample distance to be in the range of ångströms.

Figure 2.10 shows simplified schematics of an STM set-up. It summarizes the aforementioned measurement procedure and the interactions between different components. The scanning movements in x and y directions as well as the z adjustment are carried out using piezoelectric crystals [1]. Applying an electric field to a piezoelectric material changes its lattice strain, causing deformations. This is used to achieve the ångsröm-scale movements needed for both atomic resolution scans and height alterations. In addition, STM features a system for coarse motion, i.e. for bringing the tip into the vicinity of the sample, retracting it, or changing the area on the sample surface. Furthermore, for stable operation the set-up needs to be equipped with vibration isolation. This is carried out by mounting the sample stage and the scan head on springs. Elimination of sources of external resonances, such as pumps and fans may also be required. As such, STM does not necessitate UHV conditions, but they may be needed in order to prevent contamination of the sample, as is the case in this work as well.
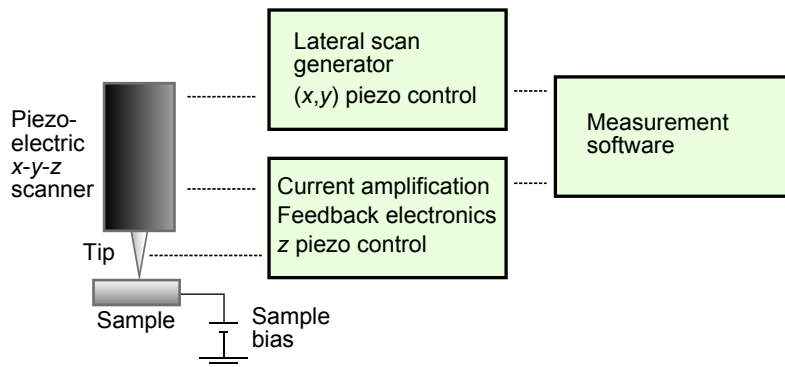
Figure 2.10. The main parts of a STM set-up are sample bias required for tunnelling current, a piezoelectric scanner capable of ångström scale movements, a feedback loop adjusting the tip height, and a $x - y$ scanning unit.

Although the working principle presented here is enough for interpreting STM results cursorily, a more thorough understanding requires advanced theory. In particular, the assumption that the tunnelling current depends solely on the tip-sample distance is not true in general. The local density of states (LDOS) i.e. the density of available electronic states in the vicinity of the tip affects to the current. Therefore, an STM image

actually convolutes geometric and electronic features. It can be derived that the LDOS of the sample is linearly proportional to the derivative of tunnelling current with respect to the sample bias. Scanning tunnelling spectroscopy (STS) is based on this. It can be used to obtain essential information of local electronic properties. The working principle of STS can be derived from Bardeen's theory and Tersoff-Hamann approximation [64].

2.5 Temperature programmed desorption

Temperature-programmed desorption (TPD) is a technique for determining desorption mechanisms and temperatures of adsorbates. Simultaneously, it also gives indirect information on the preceding adsorption. The technique is based on the theory of thermal desorption and particle detection by the means of mass spectrometry.

In an TPD experiment, the sample initially at temperature T_0 is heated with a linear heating rate β so that

$$T(t) = T_0 + \beta t. \tag{2.30}$$

As discussed in Chapter 1, the elevated temperature gives rise to desorption of the adsorbates. Desorption rate is given by equation 1.2. Since the desorbing particles are detected by the partial pressure p they induce, a relation between desorption rate and pressure is required. This is derived from the pumping equation

$$V\frac{\mathrm{d}p}{\mathrm{d}t} = Q - Sp, \tag{2.31}$$

where S is the pumping speed, V is the UHV volume and p is the pressure therein. Q is the gas load incorporating the desorbing and leaking particles that contribute to the UHV pressure. In practice, the pumping equation states that the growth rate of the UHV chamber pressure is proportional to the difference of the incoming gas load and the gas load pumped away, the difference being zero in equilibrium. In a TPD experiment, the gas load Q is caused by the thermally activated, desorbing adsorbates. Therefore, equation 2.31 can be rewritten as

$$-A\frac{\mathrm{d}\Theta}{\mathrm{d}t} = \frac{V}{k_{\mathrm{B}}T}\left(\frac{\mathrm{d}p}{\mathrm{d}t} + \frac{Sp}{V}\right), \tag{2.32}$$

where A is the sample surface area. Since pumping speed tends to be relatively high in practice, the linear term with respect to p dominates,

giving

$$p \propto -\frac{\mathrm{d}\Theta}{\mathrm{d}t}. \tag{2.33}$$

Thus, equation 1.2 is sufficient for explaining the features of TPD curves. Increase of temperature gives rise to exponential growth, but since the coverage Θ decreases gradually to zero, the growth is limited and eventually the desorption rate must drop to zero as well. Therefore, TPD curves always feature a peak. The temperature for maximum desorption rate T_{peak} is a result directly given by a TPD measurement. It can be further used to determine the value of desorption energy by using the empirical Redhead's formula

$$E_{\mathrm{d}} = k_{\mathrm{B}} T_{\mathrm{peak}} \left(\ln \frac{\nu T_{\mathrm{peak}}}{\beta} - 3.64 \right). \tag{2.34}$$

Here, ν is the attempt frequency, usually approximated as $\sim 10^{13}\ \frac{1}{\mathrm{s}}$. Multiple TPD measurements with varying coverages also give information of the order n of the desorption, since T_{peak} tends to remain constant when $n = 1$ (figure 2.11a) but decrease as a function of coverage when $n > 1$. [1, 65]
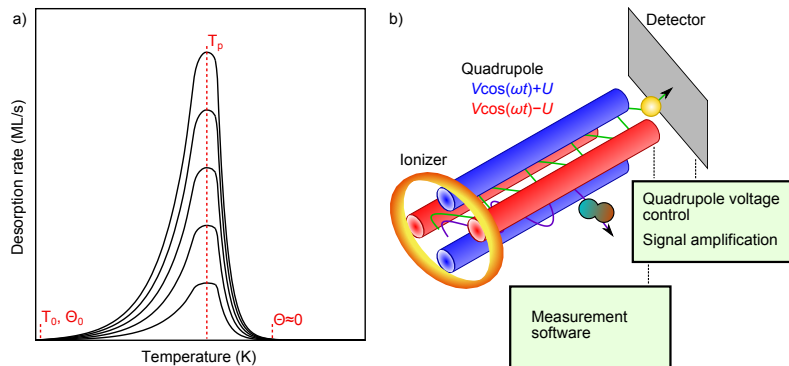
Figure 2.11. (a) A hypothetical example of first order desorption. The curves follow Polanyi-Wigner equation. A larger coverage increases desorption rate but does not change energetics. (b) TPD measurements require a mass spectrometer. A quadrupole mass spectrometer features an ionizer and a electric quadrupole, letting only ions with a wanted mass to charge ratio pass through into a detector.

To perform TPD, the experimental set-up needs to be equipped with sample heating, a temperature measurement device and a mass spectrometer, all of which are standard features in a UHV system. Moreover, to prevent error sources, heating of any chamber part other than the sample should be as limited as possible. Figure 2.11b shows schematics for a quadrupole mass spectrometer (QMS). A molecule desorbed form

the surface travels near the hot filament and is ionized by an electron. The quadrupole consists of two pairs of metal rods. Each pair is in a different, alternating potential triggered by a combination of AC and DC voltages [66]. The potentials are chosen so that only ions with a certain mass-to-charge ratio m/z will have a trajectory leading into the detector. In the detector, the signal is electrically amplified and converted into partial pressure, i.e. the part of the UHV chamber pressure caused by particles of a certain m/z, which again is directly their molecular mass, given that the particles are only once ionized.

As many molecules have the same mass, CO and N_2 ($m = 28$) being a notable example, different particles cannot always be distinguished by the mass of the initial molecule. However, due to the hot filament bond breaking may also take place, splitting the molecule and giving thus rise to minor peaks of different m/z. Therefore, in a p vs. m/z measurement, certain molecules will cause a characteristic set of peaks with known intensity ratios. This can be used in order to distinguish peaks originating from different sources. This molecule dissociation caused by the QMS ionizer must not be confused with dissociative desorption, where the bond-breaking of molecules takes place already at the surface.

2.6 The experimental set-up

The experimental work for this thesis was carried out using three ultra high vacuum (UHV) systems. XPS, TPD and LEED measurements for Publications I–III were performed with an in-house built chamber system featuring a dual-anode X-ray gun, a hemispherical analyzer and an ion gun by Physical Electronics, LEED optics by Princeton Research Instruments, and a quadrupole mass spectrometer by Stanford Research Systems. The system also features sample cooling with liquid nitrogen. Sample heating was initially resistive but the change of the sample manipulator enabled electron beam heating in experiments for Publication III. The base pressure of the system was around 10^{-10} mbar, provided by ion, turbomolecular and titanium sublimation pumps. For precursor introduction, the system was equipped with a gas line network linked to the chamber through a leak valve.

The STM studies reported in Publications II and III were performed in another in-house built UHV system, equipped with LEED optics by Omicron, an ion gun by Varian and AES by Physical Electronics. The

STM was provided by RHK in Publication II and replaced by Omicron VT in Publication III. The system also featured a load-lock and sample storage, nitrogen cooling and e-beam heating, and a similar gas line for precursor introduction. The base pressure in this system was below 10^{-10} mbar.

The XPS work for Publications IV-VII was carried out with a commercial Surface Science Instruments SSX-100 system. The X-ray gun produces monochromatic aluminum K_α radiation, and the photoelectrons are collected by a hemispherical analyzer. In addition, the system is equipped with an electron flood gun to compensate the loss of photoelectrons and to prevent charging of insulating samples. The base pressure of this system was 10^{-9} mbar during the reported experiments.

2.7   Sample preparation

The platinum (111) and (110) single crystals were produced and polished by MaTeck. Prior to experiments, they were cleaned in UHV using repeated cycles of sputtering with Ar^+ ions and annealing at elevated temperatures. The exact cleaning recipes can be found in the respective publications. XPS and LEED were used in monitoring the surface quality, and cleaning was continued until photoelectron lines originating from adventitious carbon and adsorbate species were observed to vanish and the diffraction pattern of a clean surface was bright. Platinum has a face-centered cubic (fcc) crystal structure with a lattice constant of 3.924 Å [67]. A clean Pt(111) surface is hexagonal and close-packed but Pt(110) forms a 1×2 missing row reconstruction [68, 69]. Figure 2.12 shows the clean surface structures.

Maleic anhydride appears as solid crystalline flakes in standard ambient conditions. In order to evaporate maleic anhydride molecules in gas phase, the solid source material was placed in a container and heated in a water bath up to ca. 345 K. This is 20 K above the melting point of maleic anhydride [70] and found enough for evaporation of maleic anhydride molecules. The container was connected to a variable leak valve, and the pressure in the line was pumped down to 10^{-1} mbar before each experiment. The leak valve was used to backfill the chamber, and a QMS was employed to monitor the magnitude of the exposure. The Pt crystal was kept at 170 K during the deposition.

Phosphorus introduction was carried out with a similar set-up. A steel
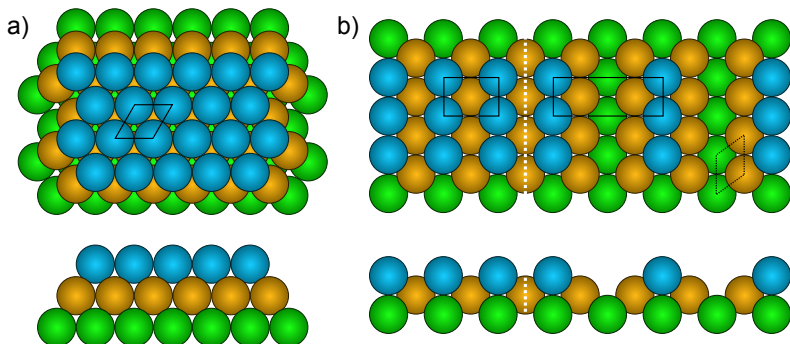
Figure 2.12. (a) The (111) facet of a platinum crystal features close-packed atoms. Neighbouring hollow sites differ due to alignment of the second and third rows. (b) The (110) facet of platinum has a rectangular unit cell with a $\sqrt{2} : 1$ ratio (left). To minimize surface energy, the facet forms a 1×2 reconstruction (right) which consists of (111) microfacets.

container was filled with red phosphorus powder and heated with a hot-air gun. The achieved air temperature was roughly 900 K, enough to evaporate P_4 molecules out of the solid source with a vapour pressure larger than 1000 mbar. The P_4 gas was then led into the UHV chamber through a leak valve. The gas was guided through a tube and directed towards the sample surface, facing the tube end. This enabled significantly larger local exposures without contaminating the chamber walls with phosphorus. The phosphorus introduction process is an example of chemical vapour deposition (CVD) [71]. The P_4 molecules functioned as precursors, forming a well-defined phosphorus coating on the surface, as will be discussed in detail in Chapter 3.

The automotive catalyst materials characterized in this work were all commercial models or prototypes manufactured by Dinex Ecocat (figure 2.13). As an active material they had either platinum or a mixture of palladium and platinum. The support was either alumina (Al_2O_3) or silica-zirconia (SiO_2-ZrO_2) mixture. The laboratory-scale deactivation treatments were carried out in a flow reactor at University of Oulu. Table 2.1 lists the studied catalyst materials and 2.2 the used treatment parameters. For XPS measurements, catalyst washcoat was scraped from the surface of a honeycomb and pressed on an indium chip to inhibit charging effect during the measurements. The inlet and outlet parts, with respect to the sample orientation in the flow reactor, were treated and measured separately.
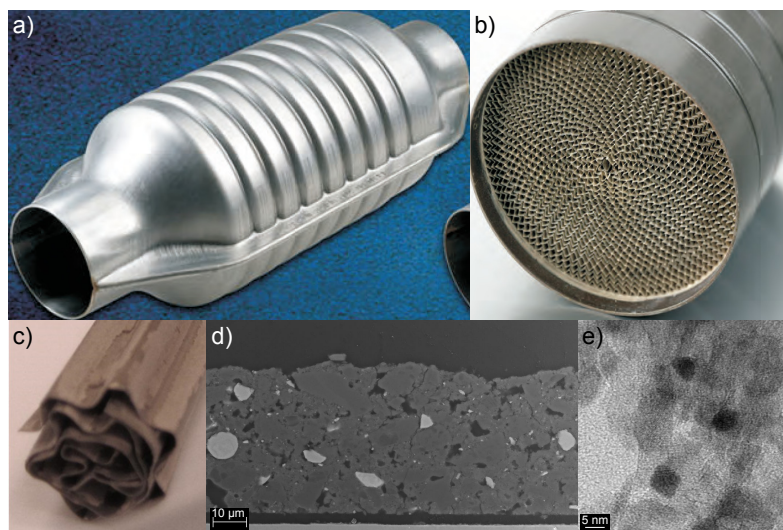
Figure 2.13. The basic structure of the automotive catalysts studied in this work. (a-b) The catalytic converter is a steel shielded honeycomb. (c-d) The honeycomb surface has been coated with a porous washcoat and (e) the catalytic metal itself is dispersed in the washcoat, represented by the dark features in the transmission electron microscopy image.

Table 2.1. A list of catalyst and support samples studied in this work. The weight ratios of active metals have been marked in parentheses.

Description	Active metal	Support	Additive oxides
A low-loading catalyst for diesel oxidation	Pt, Pd (4:1)	Al_2O_3	Ce, Zr, Si, Ti
A low-loading catalyst for diesel oxidation	Pt	Al_2O_3	Ce, Zr, Si, Ti
The washcoat for the previous two	-	Al_2O_3	Ce, Zr, Si, Ti
A high-loading catalyst for natural gas oxidation	Pt, Pd (1:4)	Al_2O_3	-
A low-loading catalyst for diesel oxidation	Pt	SiO_2, ZrO_2	-

Table 2.2. A list of the aging treatments carried out for the measured samples.

Ref.	Description	Treatment gas composition
fresh	As-received	
SW	Sulfur poisoning	100 ppm SO_2, 10% H_2O, 10% air, ca. 80% N_2
LPW	Phosphorus poisoning, low phosphorus concentration	10% H_2O with 0.065 mol/l $(NH_4)_2HPO_4$, 10% air, ca. 80% N_2
HPW	Phosphorus poisoning, high phosphorus concentration	10% H_2O with 0.13 mol/l $(NH_4)_2HPO_4$, 10% air, ca. 80% N_2
PSW	Phosphorus-sulfur poisoning	100 ppm SO_2, 10% H_2O with 0.13 mol/l $(NH_4)_2HPO_4$, 10% air, ca. 80% N_2

3.   Results

3.1   Maleic anhydride on platinum (111)

Adsorption and desorption of maleic anhydride (MA) on a platinum (111) surface was studied experimentally using mainly XPS and TPD. XPS was used to detect temperature induced chemical changes in the adsorbed species and TPD was employed to determine the desorption behaviour in a wide temperature range. To complement these, adsorption and desorption were also simulated using density functional theory. The study is reported in Publication I.
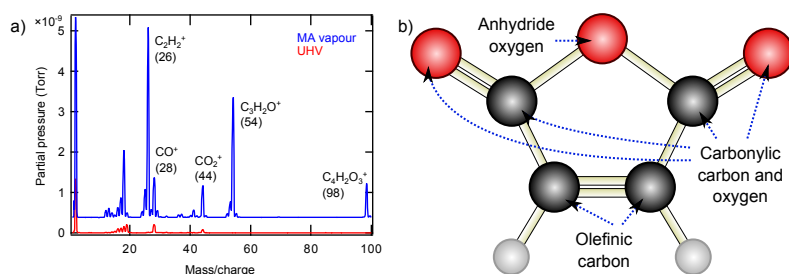
Figure 3.1. (a) The mass spectrum of maleic anhydride vapour features multiple peaks caused by maleic anhydride molecules themselves and their fractions. (b) A maleic anhydride molecule is planar and cyclic. The differently bonded carbon and oxygen atoms give rise to distinct photoelectron lines.

The MA exposure was monitored with a mass spectrometer using the characteristic set of m/z peaks of MA shown in figure 3.1a as a fingerprint. In XPS, MA gives rise to four distinct peaks caused by olefinic and carbonylic carbon atoms and anhydride and carbonylic oxygen atoms (figure 3.1b). Deposition on a Pt (111) surface at room temperature was seen not to cause MA adsorption, as XPS and TPD both indicated only presence of some impurity CO. Therefore, all subsequent exposures were carried

out at 170 K in a range from 0.8 L to 15 L. In XPS, the four peaks are visible following the stoichiometric ratios of a maleic anhydride molecule. MA intake grows linearly up to 4 L above which the rate of growth moderately decreases. This was attributed to the beginning of a multilayer growth phase. The coverage after a 4 L deposition was estimated to be 0.28 monolayers. Even at 15 L, the coverage showed no traces of saturation. In addition, LEED did not show any ordered structures. Figure 3.2 summarizes the behaviour of MA at different exposures.
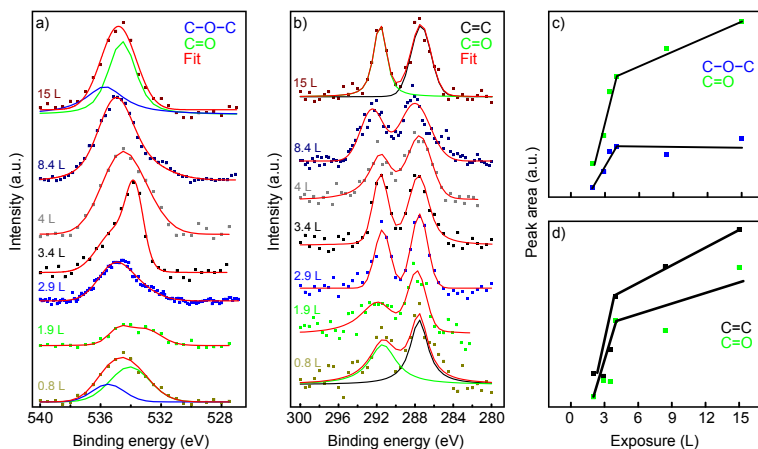
Figure 3.2. (a) O 1s and (b) C 1s spectra of the MA/Pt(111) surface after various exposures. (c) The growth in intensity (area) of the two O 1s XPS lines as a function of MA exposure. (d) The same for C 1s.

Spin-polarized and spin-restricted DFT calculations with the VASP software were employed to have insight into the adsorption geometry and energetics of the MA molecules. Details of the used techniques are available in Publication I and eg. references [72–74]. Di-σ bonding through the two olefinic carbon atoms was found to be the most favourable adsorption mode. Each of the two carbon atoms form a σ bond with the nearest substrate atom. Changes in the C−C−H bond angles and the olefinic bond length suggest that the hybridization of carbon atoms changes from sp^2 to sp^3. The adsorbed molecule is relaxed on the surface in an oblique angle, as illustrated in figure 3.3. The binding energy for an MA molecule was found to be -95 kJ/mol with deviations of roughly ± 10 kJ/mol depending on simulation parameters.

After MA deposition, its behaviour at increasing temperatures up to 600 K was studied with XPS and TPD. The adsorbed species remain intact below 185 K. XPS scans between 185 and 240 K indicate a 60-65 percent
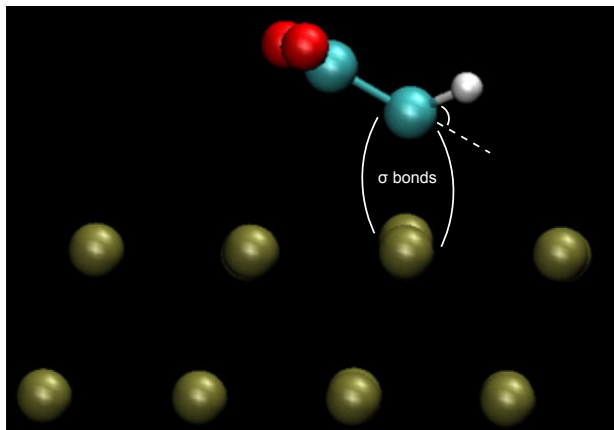
Figure 3.3. A maleic anhydride molecule prefers σ bond formation between the olefinic carbon atoms and the nearest platinum atoms. The planar configuration of the molecule experiences some distortion.

loss of all adsorbed species (figure 3.4). In addition, the 1s line for olefinic carbon starts to broaden significantly. This was attributed to opening of the molecular ring, and further to dissociation of the undesorbed MA molecules. The losses are in agreement with TPD results which show a desorption peak around 240 K. The desorption curves of m/z values 26, 28, 44, 54 and 98 were measured, and while their ratios were mostly in accordance with the QMS fingerprint shown in figure 3.1a, excess of $C_2H_2^+$ was observed. This predicts also dissociative desorption taking place, which again is in agreement with the interpretation of changes in the XPS spectra. Since the peak form of the $C_2H_2^+$ and MA^+ curves were however qualitatively similar, it can be assumed that desorption at 240 K is mainly molecular. The behaviour was similar regardless of the exposure, which was varied between 1 to 15 L, albeit the growth rate of desorption yield is weakened above 4 L, similarly to what was observed in XPS peak areas. The desorption energy, as estimated with equation 2.34, was 80 kJ/mol. The binding energy for MA is thus -80 kJ/mol which is close to the value given by DFT calculations.

Between 240 and 370 K, roughly 10% decrease in peak areas was seen in XPS indicating more desorption. Furthermore, the stoichiometric ratios were distorted, which suggests further dissociation of the MA molecules. This is again confirmed by TPD, showing CO^+ and CO_2^+ ions to desorb around 360 K. Other m/z values, especially 98, did not peak at all. Therefore, carbon monoxide and dioxide most probably originate from decomposed MA molecules on the surface.
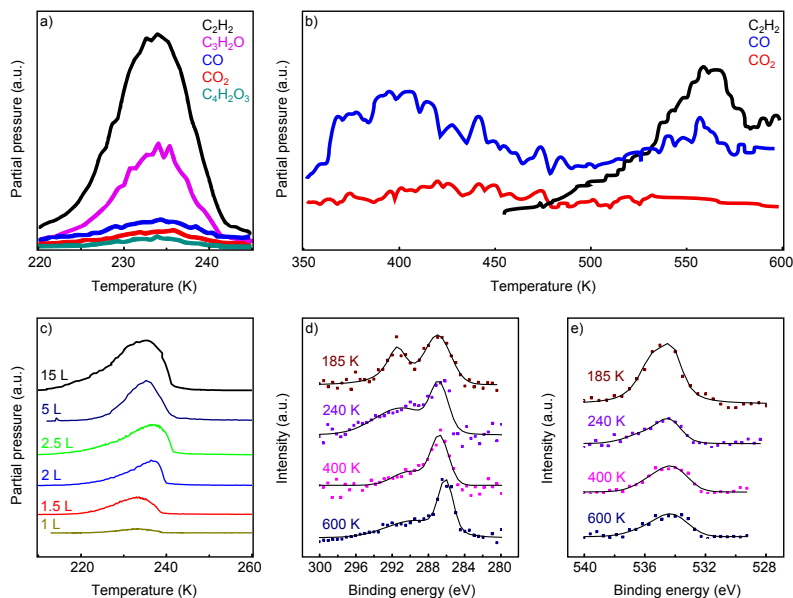
Figure 3.4. (a) The major desorption takes place at $220-240$ K. In this region, desorption is predominantly molecular, although C_2H_2 desorption takes place as well. (b) At higher temperatures, smaller desorption peaks of MA fragments CO, CO_2 and C_2H_2 are observed, but intact molecules are not. (c) The desorption yields grow as a function of coverage. The peak temperature remains, indicating molecular desorption. (d) C 1s and (e) O 1s spectra show coverage decrease when temperature rises. The distortion of peak ratios indicates dissociation.

The peak areas decrease ca. 15% when the temperature is increased from 370 K to 600 K. Above 500 K, TPD peaks were found for ethyne, carbon monoxide and carbon dioxide, but again, not for complete MA molecules. This further indicates all MA was either desorbed or dissociated already at 240 K. These desorption peaks could not be detected in every measurement, and their origin was attributed to surface defects caused by sputtering. This was verified by DFT simulations on MA molecule adsorption in presence of vacancies on the topmost surface layer. A di-σ bound molecule on a vacancy was found to have a binding energy of -156 ± 6 kJ/mol, agreeing with the experimentally gained value -155 kJ/mol.

Above 600 K, no further desorption peaks were observed. In XPS, some residual carbon and oxygen were seen to be left on the surface, probably as CO and atomic oxygen. Figure 3.5 summarizes the temperature dependent behaviour of maleic anhydride on platinum (111).
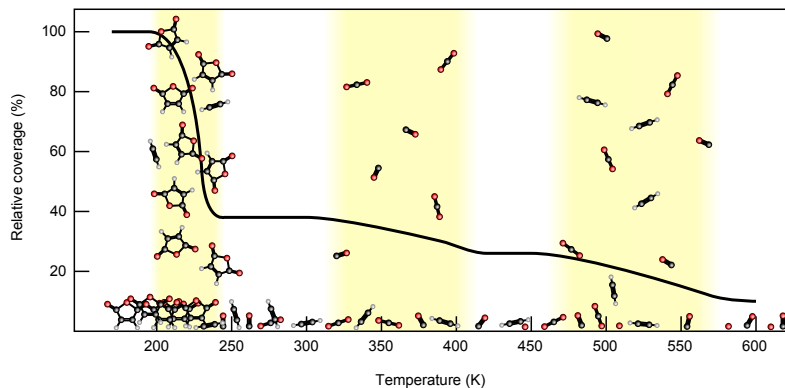
Figure 3.5. An illustration of the MA coverage over the measured temperature range. Most of the desorption takes place below 240 K. Above, no intact MA molecules can be observed. Two wide regions of desorption appear at higher temperatures. The detailed dissociation process and intermediate moieties on the surface were not characterized in this work.

3.2 Phosphorus on platinum (111)

Gaseous phosphorus was deposited on a platinum (111) single crystal surface with CVD. STM and LEED, together with DFT simulations, were employed to determine adlayer structures. In addition, poisoning effect on carbon monoxide adsorption was studied with XPS and TPD. The results are reported in Publication II, excluding the unsaturated adlayer structures which are presented here.

Red phosphorus powder was evaporated at 900 K and the vapour was introduced into UHV through a leak valve. At that temperature, phosphorus vapour consists mainly of P_4 molecules [75]. In QMS, the major peak given by phosphorus vapour was at 31. This was used to measure the exposure in all experiments. However, since the vapour was guided towards the sample through a tube, the local exposure on the platinum surface was estimated to be roughly 200 times higher. In XPS, P 2p and Pt 4f were measured, and the ratio of their peak areas was regarded as the measure of phosphorus coverage.

Phosphorus intake was calibrated with depositions in various temperatures. As shown in figure 3.6a, higher surface temperature was seen to result in larger phosphorus coverage. This suggests the adsorption reaction needs to be activated. By XPS, the sticking was estimated to be roughly seven times higher at 720 K than at room temperature. In addition, above 970 K phosphorus starts to desorb, as shown in figure 3.6b. Therefore, 720 K was chosen as the surface temperature for all subse-
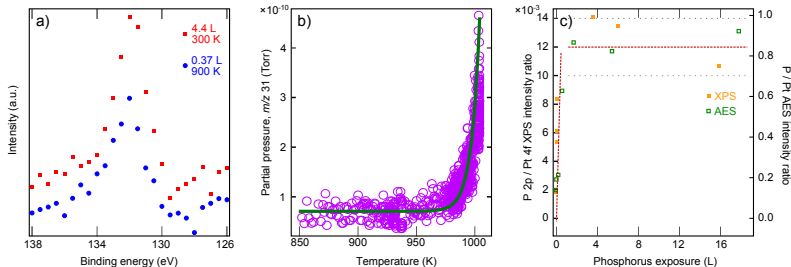
Figure 3.6. (a) P 2p spectra after two depositions show that sticking increases at elevated temperatures. (b) A TPD spectrum of phosphorus shows desorption above 970 K. (c) Phosphorus coverage increases as a function of exposure until a saturation limit is reached. The axis shows the exposure as measured, but the local exposure is estimated to be 200 times higher.

quent deposition experiments.

Phosphorus coverage saturates, when the exposure exceeds 1 L, indicating a local dose roughly around 200 L, as shown in figure 3.6c. The saturated P to Pt ratio is 0.020±0.002. In comparison, for a monolayer of phosphorus atoms, the ratio estimated by equation 2.8 is 0.015. The saturated coverage does not form a properly well-ordered structure, as LEED shows only a few very dim spots. To obtain an ordered structure, the surface was annealed at 1020 K for 2 min. This decreased the coverage by ca. 40%, giving a P to Pt XPS ratio of 0.012±0.002. Phosphorus signal weakening is mostly due to desorption, although diffusion into the platinum bulk may also take place [76].

The saturated and annealed phosphorus adlayer has a $4\sqrt{3} \times 4\sqrt{3} - \text{R}30°$ symmetry, as shown by the LEED pattern in figure 3.7a. The unit cell consists of two three-pointed clusters which form a symmetric hexagonal pattern when extended over the x-y plane, as seen in the STM image in figure 3.7b. The pattern remains constant over wide terraces, and no dislocations were observed. Based on the physical size of the clusters and the observed P to Pt XPS ratio, the clusters were considered to be more complex than the initial P_4 molecules. This is also supported by the fact that elevated temperatures are needed to obtain the structure. The lower areas between the clusters feature smaller, possibly moving units.

Dispersion-corrected DFT calculations with generalized gradient approximation and AIMPRO code were performed to gain more insight into the adlayer structures [74, 77]. The adsorbed species were determined by simulating the adsorption of several possible phosphorus clusters. Based on the results, P_{13} or P_{14} clusters are the most likely candidates to explain
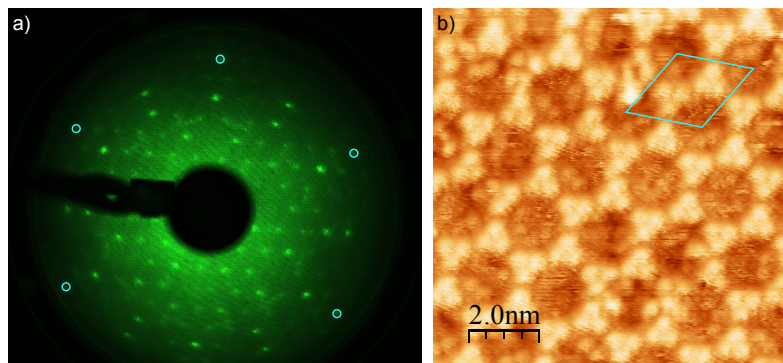
Figure 3.7. (a) The LEED pattern of the saturated phosphorus adlayer at 56 eV shows a $4\sqrt{3} \times 4\sqrt{3} - \mathrm{R}30°$ symmetry. There is only one domain, since the reciprocal lattice is conserved in $120°$ rotations and reflections over the main axes. The first order diffraction maxima of the substrate are highlighted. (b) The STM image (62 mV, 420 pA) of the saturated phosphorus adlayer shows three-pointed clusters forming hexagons. Drawn boundaries of a unit cell are visible in the upper right corner.

the experimental results. As figures 3.8a-c shows, these are formed by binding three P_4 molecules to a single phosphorus atom or a P_2 dimer, respectively. Although neither of the clusters is stable in vacuum, both of them remain intact when bound to Pt(111). A P_{13} cluster has a binding energy of 7.15 eV and is totally symmetric, whereas P_{14} becomes slightly twisted and has a binding energy of 6.16 eV. The energetic preference for P_{13} is due to the weakly bound fourfold coordinated central atoms in the P_{14} molecules. P_{14} occupies on-top sites, while P_{13} prefers bridge sites, as shown in figures 3.8b-c. Figures 3.8d-e present a simulated STM pattern of P_{13}, without the platinum slab, and its comparison with an experimental STM scan. These match completely, and also the pattern produced by P_{14} is virtually identical. Based on Bader analysis [78], the charge transfer from P_{13} and P_{14} to the substrate is $0.80e$ or $0.86e$, respectively.

The additional features in the holes can be explained by trapped P_4 molecules, as shown in figure 3.8d. A layer of the hexagonal structure together with these added P_4 units gives rise to a P to Pt ratio in agreement with XPS. Thus, this may be the complete picture of the saturation structure. However, substitutional phosphorus atoms in the topmost platinum layers are also possible.

Adlayer structures below the saturation limit have also been studied tentatively. At coverages lower than 25 percent of the saturated coverage, no ordered adlayers can be detected. LEED shows a bright 1×1 diffraction pattern of the platinum substrate. In STM scans, unordered features are
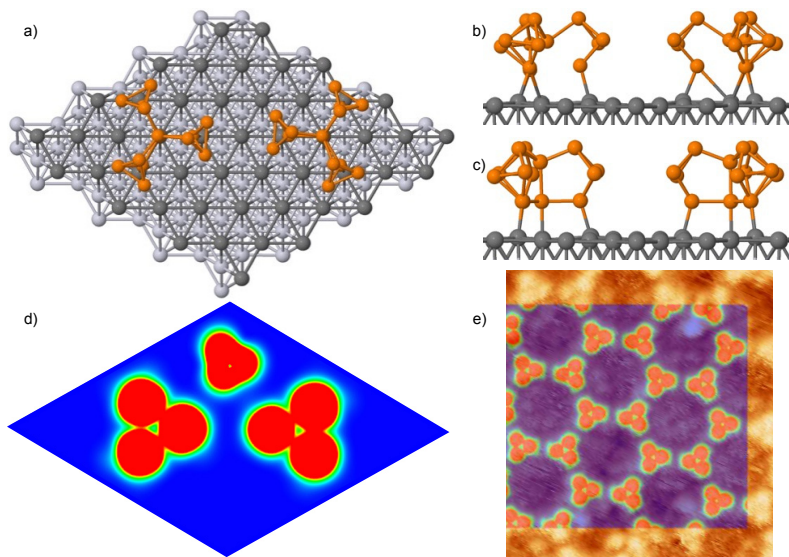
Figure 3.8. (a) Top view of two P_{14} clusters relaxed in the adlayer unit cell, as simulated with DFT. (b) Side view of two P_{13} and (c) P_{14} clusters. (d) A simulated STM image of the unit cell, including a trapped P_4 molecule (-2 V). (e) Simulated and actual STM images matched together.

visible near terrace steps of the platinum substrate. At higher coverages, ca. $40-80$ percent of the saturation limit, LEED shows a $\sqrt{7} \times 9$ structure, as illustrated in figure 3.9. Since the unit cell of such adlayer is not aligned along the symmetry axes of the substrate, the LEED pattern has six domains. Likewise, there are six equally possible growth directions, all having the same symmetry, in the real lattice as well. STM scans show that the adlayer consists of stripes of adsorbates growing along the directions predicted by LEED. The distance between two nearest adsorbates is, within the limits of error, $\sqrt{7}$ times the lattice constant, as also given by LEED. However, the stripes are located seemingly randomly so that the distance between two stripes is not nine times the lattice constant, as LEED would suggest. Thus, the measured sample, or at least the particular location, was not completely ordered. The nature of the adsorbates was not determined, but based on their size they can possibly be P_4 molecules or P_3 trimers. STM also suggests that the stripes enclose areas with adsorbates, whereas the darker areas are likely platinum. The lighter areas are not well-ordered here, but in some LEED measurements the stripes and the saturated structure have been seen to co-exist, which may take place similar way.

Catalytic poisoning by phosphorus was studied by dosing carbon monox-
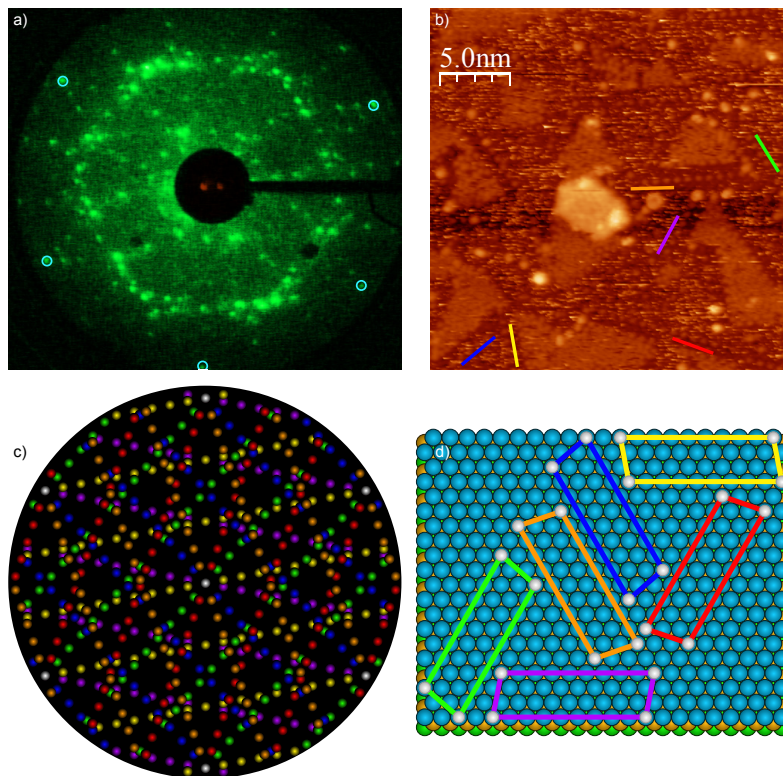
Figure 3.9. (a) The LEED pattern of phosphorus adlayer below saturation (65 eV) presents a $\sqrt{7} \times 9$ symmetry in six domains. (b) An STM image (107 mV, 167 pA) of a partially ordered P-Pt surface below saturation. There are adsorbate lines growing in six directions and triangular areas of adlayer growth, presumably. (c) An ideal representation of the reciprocal lattice with six domains. (d) The corresponding six unit cell directions in the real lattice.

ide at room temperature on a Pt(111) surface pre-covered by phosphorus. The amount of adsorbed CO was studied by measuring C 1s line with XPS and CO^+ (m/z 28) desorption near 370 K. The results are in figure 3.10, and both techniques indicate linear decrease of CO intake as a function of phosphorus coverage. At phosphorus saturation, CO does not adsorb at all.

3.3 Phosphorus on platinum (110)

Phosphorus adsorption was studied also on the platinum (110) single crystal surface using XPS, LEED and STM. The aim of these studies was to determine how the phosphorus coverage depends on the exposure, and to characterize the ordered adlayer structures. The results are reported in
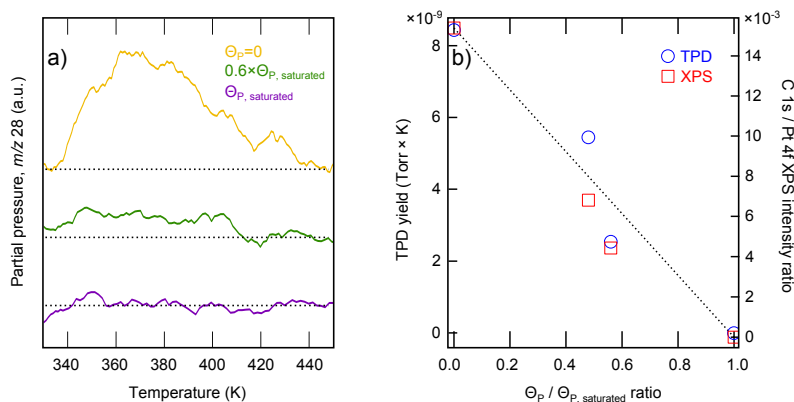
Figure 3.10. (a) Examples of carbon monoxide desorption spectra at different phosphorus coverages. (b) The CO intake decreases to zero as a function of phosphorus coverage, as determined by both TPD and XPS.

Publication III.

The deposition method was exactly the same as described for the P/Pt(111) system in the previous section. The P 2p vs Pt 4f peak area ratio was again used as the measure of phosphorus coverage. The ratio of 0.009 was estimated to correspond to one monolayer. The value is smaller than for the Pt(111) surface due to the sparser structure. A deposition carried out at the room temperature resulted in a significantly lower intake than at 720 K, and thus, all further depositions were performed at 720 K.

The phosphorus did not form ordered structures as deposited, and therefore the surface was annealed after the exposure at 970 K for 2 min. By XPS, annealing removed roughly 30% of the phosphorus coverage. The coverage as a function of exposure after annealing the surface is shown in figure 3.11. The plot shows that saturation takes place near three monolayers. The saturation coverage is obtained with exposures greater than 8 L (1600 L locally).

After annealing LEED studies showed that phosphorus had formed well-ordered superstructures on the surface. Three different adlayer symmetries were found, depending on phosphorus coverage, as can be seen in figure 3.11. Figure 3.12 shows the LEED patterns of these adlayers. The 2×3 symmetry in figure 3.12a was obtained with XPS intensities roughly corresponding to 1 monolayer. The characteristic 1×2 reconstruction of the Pt(110) surface is not conserved in the adlayer formation. However, a new 1×3 reconstruction is possible, but this cannot be verified with simple LEED analysis. Due to the relatively small size of the superstructure unit cell, the phosphorus species on the surface are likely to be single
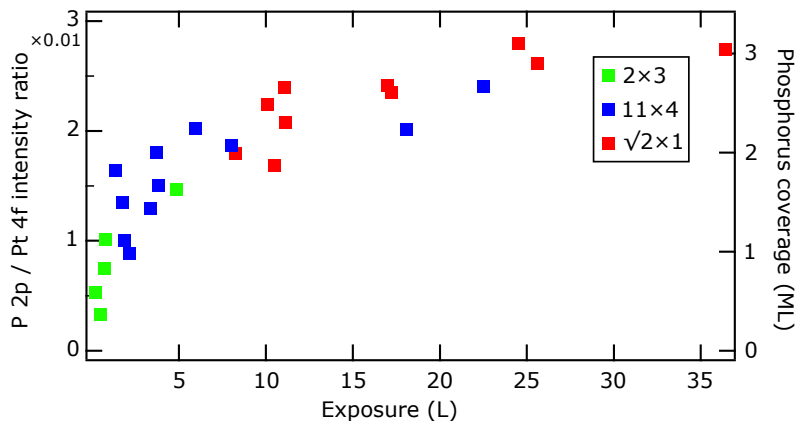
Figure 3.11. The phosphorus coverage on Pt(110) as a function of exposure after anneal-
ing the surface. The exposure has been calculated using the partial pressure
backfilling the UHV chamber, and therefore the local exposure is estimated
to be 200 times higher. The different colours correspond to different adlayer
structures.

atoms, or P_2, P_3 or P_4 particles. The coverage of 1 ML indicates that the
unit cell contains roughly six phosphorus atoms. The 11×4 structure
in figure 3.12b was seen at coverages of roughly 2 monolayers. The sig-
nificantly larger unit cell gives much more possibilities for the nature of
the adsorbed species. Figure 3.12c shows the saturation structure corre-
sponding to ca. 3 monolayers. The observed symmetry $\sqrt{2} \times 1$ refers to
an incommensurate square lattice, adopting its lattice constant from the
longer unit vector of the platinum substrate. Although the size and the
symmetry were found to be always the same, the orientation of the super-
structure varied. The two variations found most often were the adsorbate
lattice vectors being parallel to the substrate unit vectors, and a rotation
of 45 degrees. These two are visible also in figures 3.12c-d. However, some
other rotations were found as well. In addition, the substrate spots could
not be seen with LEED (except for those coinciding with adlayer-induced
spots). This suggests there is a multilayer of phosphorus on the surface.
Furthermore, since the unit cell is so small, the adlayer structure consists
probably of phosphorus atoms or P_2 dimers. As figure 3.11 shows, cover-
age regions for different superstructures overlapped, and similarly, mul-
tiple adlayer symmetries could also be seen simultaneously with LEED.

The 11×4 and $\sqrt{2} \times 1$ superstructures were also studied with STM.
As shown in figure 3.13a, the 11×4 structure forms rectangular sheets.
Their size depends probably on the underlying platinum terraces. As the
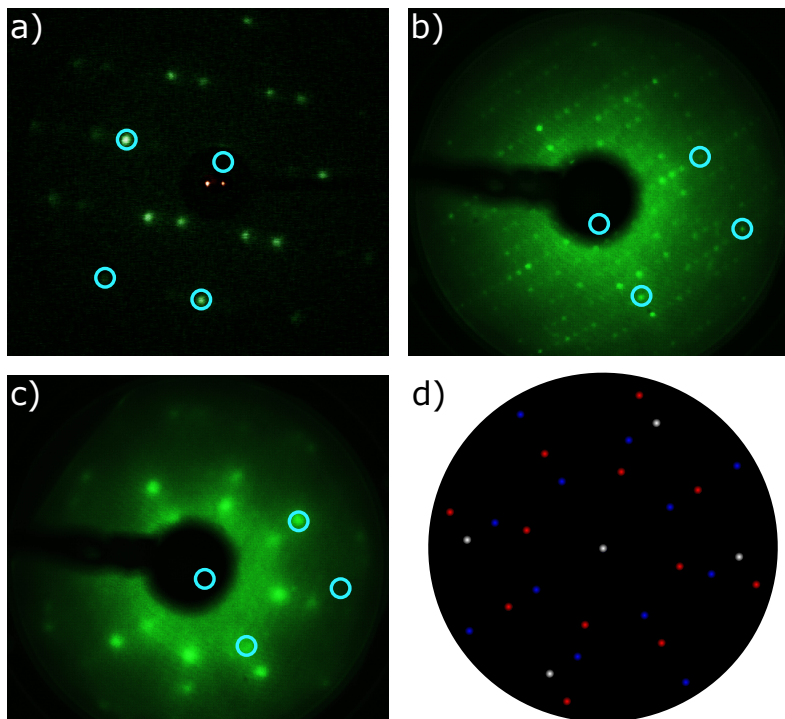
Figure 3.12. Different LEED patterns caused by P/Pt(110) superstructures. The 1×1 substrate spots are highlighted. (a) The 2×3 structure at 97 eV. (b) The 11×4 structure at 100 eV. (c) The $\sqrt{2} \times 1$ structure with two domains at 130 eV. (d) The reciprocal lattice of the $\sqrt{2} \times 1$ structure with two domains having rotations of 0 and 45 degrees.

inset with higher resolution shows, the adsorbates seem to form large clusters on the surface. Some of the features imply weakly that the clusters may be triangularly shaped, not unlike the P_{13} or P_{14} clusters seen on Pt(111). The STM images show also lines extending through the rectangular sheets. However, as the unit cell drawn in the inset in figure 3.13a indicates, the lines do not follow any symmetry observed in LEED, possibly because the separation between two lines was observed to vary. The lines are probably caused by the phosphorus clusters and the structures underneath them. In addition to the sheets, areas regarded as clean Pt(110) were also observed. An STM image of the saturation structure in figure 3.13b shows a completely different topography with sheets of various shapes. Overall, the features on the surface were found to be quite uneven and irregular. The unit cell was too small to be distinguished.

Based on the findings in XPS, LEED and STM, a simple tentative model to explain the adsorption structures and their evolution is presented in figure 3.14. The basic idea is that the P_4 molecules are dissociated into
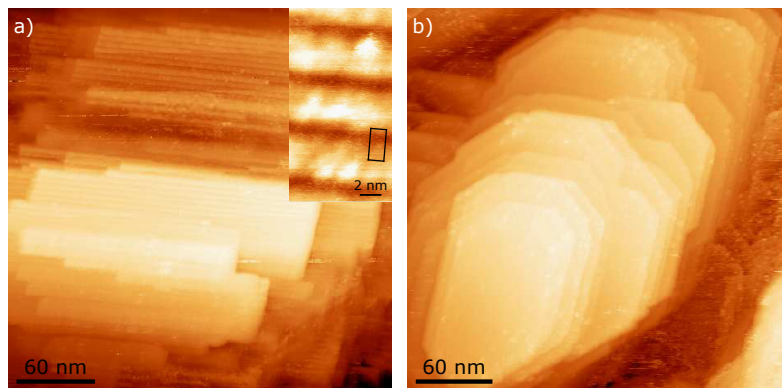
Figure 3.13. STM images of phosphorus adlayers on Pt(110). (a) The 11×4 structure appears as rectangular sheets (main image 329 mV, 130 pA, inset -630 mV, 440 pA). (b) The $\sqrt{2} \times 1$ structure appears as layers of multiple shapes (86 mV, 158 pA).

atoms, adsorbing on various sites on the surface. The more there is phosphorus, the denser is their structure. Figure 3.14a shows the model for the 2×3 structure. It consists of six phosphorus adatoms, thus being in agreement with the XPS results. It evolves into the 11×4 (figure 3.14b), when the distance between the phosphorus atoms in the $[1\bar{1}0]$ direction is decreased and the pattern is slightly skewed. Such a structure does not alone give rise to a coverage given by XPS. However, if phosphorus forms large clusters such as P_{13} or P_{14} on top of the pattern, as STM results indicate, the resulting structure agrees with XPS as well. If the atomic pattern is skewed and squeezed slightly further, the $\sqrt{2} \times 1$ symmetry shown in figure 3.14c can be obtained. To achieve the 3 ML coverage, another similar layer is needed on top of the first one. This multilayer structure explains why the substrate cannot be detected with LEED. In addition, the saturation may be explained by the surface being totally covered, which prevents interactions between platinum and phosphorus.

3.4 Phosphorus poisoning of platinum automotive catalysts

Platinum and platinum-palladium oxidation catalysts (table 2.1) were studied in collaboration with other research groups using a wide range of techniques [79]. In this work, emphasis is on the surface analysis carried out with XPS. Besides it, chemical composition within the catalyst bulk was determined with inductively coupled plasma optical emission spectroscopy (ICP-OES), and chemical bonds in the sample were charac-
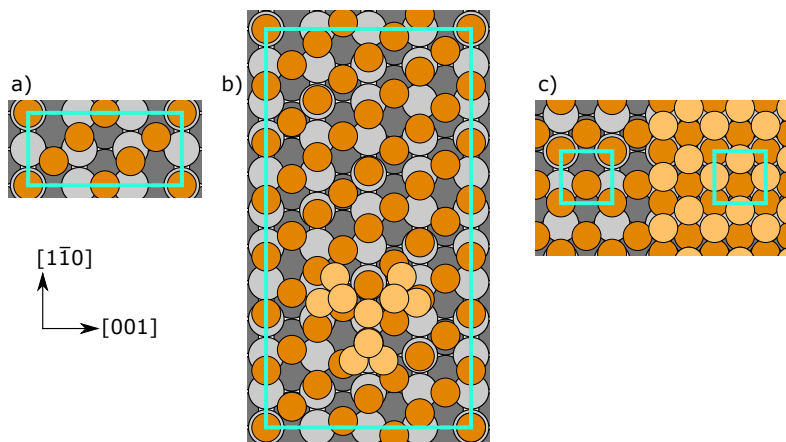
Figure 3.14. A model for P/Pt(110) adlayer structures. (a) The 2×3 structure is caused by a pattern of phosphorus atoms. (b) The 11×4 structure is achieved with a similar but denser adatom layer accompanied by large phosphorus clusters. (c) The $\sqrt{2} \times 1$ structure has an even denser pattern in multiple layers.

tarized with diffuse reflectance infrared Fourier transform spectroscopy (DRIFTS). Structure of the catalysts was studied with scanning electron microscopy (SEM) as well as transmission electron microscopy (TEM), equipped with energy dispersive spectrometer (EDS), and their phase compositions were determined with X-ray diffraction (XRD). Furthermore, Brunauer-Emmet-Teller (BET) and Barrett-Joyner-Halenda (BJH) analyses together with N_2 physisorption were applied to characterize specific surface areas and pore sizes. Perhaps most importantly, the activity of the catalysts was tested by introducing gas mixtures through the catalyst honeycombs in a flow reactor and measuring their conversion rates. Phosphorus poisoning of Pt/Al_2O_3 and $Pt-Pd/Al_2O_3$ DOCs is discussed in Publication IV and Publication V. Publication VI concentrates on phosphorus poisoning of a $Pt-Pd/Al_2O_3$ NGO catalyst, and sulfur and phosphorus poisoning of a Pt/SiO_2-ZrO_2 DOC is characterized in Publication VII.

3.4.1 Alumina supported platinum and platinum-palladium diesel oxidation catalysts

Phosphorus concentration in the $Pt-Pd/Al_2O_3$ and Pt/Al_2O_3 catalysts after LPW and HPW treatments (table 2.2) were studied with XPS, ICP-OES and SEM together with EDS. XPS was measured both at inlet and outlet ends of the catalyst samples. EDS studies showed most of the phosphorus lied within the topmost 10 micrometres from the sample surface in the HPW treated catalysts, and in the LPW treated samples practically no

phosphorus could be found deeper. However, in a bare support material, the depth distribution was found more or less uniform. XPS spectra of P 2s lines measured at inlet ends are in figure 3.15a. Phosphorus concentration at each inlet was between 9 and 12 wt.%, outlets having typically slightly less phosphorus. Phosphorus concentrations gained with ICP-OES were generally only a half of those aquired with XPS, or even less. This is because XPS measures surfaces, with densely dispersed phosphorus, whereas ICP-OES gives information on bulks.
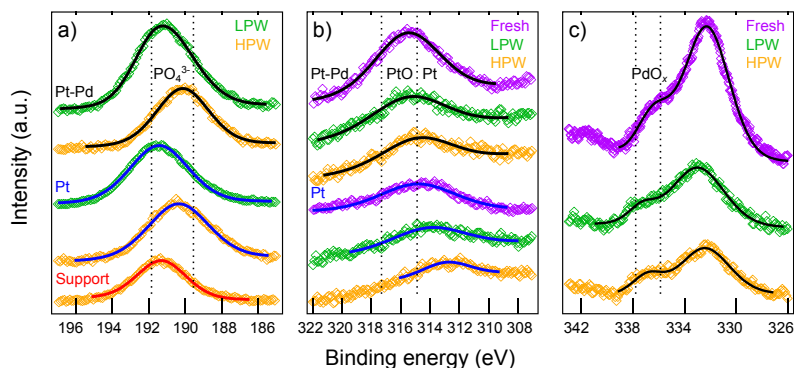
Figure 3.15. (a) P 2s, (b) Pt $4d_{5/2}$ and (c) Pd $3d_{5/2}$ photoelectron lines measured at the inlet ends of fresh and phosphorus poisoned alumina-supported platinum and platinum-palladium diesel oxidation catalysts. The Pd $3d_{5/2}$ lines share their binding energy window with the more prominent Zr $3p_{3/2}$ lines. The dashed lines represent boundaries of the binding energy ranges of the marked chemical states.

XPS, XRD and DRIFTS were used to determine the chemical state of phosphorus. XPS suggests undisclosed form of phosphate (PO_4^{3-}) [80], and XRD amorphous $AlPO_4$. DRIFTS results indicate phosphite and aluminum metaphosphate. Thus, it can be concluded that most of the phosphorus can be found in phosphate compounds, most likely with aluminum. Figures 3.15b-c show the XPS spectra of Pt $4d_{5/2}$ and Pd $3d_{5/2}$ lines. Palladium appears as palladium oxide (PdO or higher) [80, 81]. Platinum too is oxidic, or possibly hydroxidic, in the Pt-Pd catalysts, while it appears metallic in the Pt catalysts [80, 82]. Phosphorus treatments did not alter the chemical state of these noble metals. The concentration of platinum was found to be 1 wt.% or less in all samples, and Pd concentration was less than a third of that.

TEM was applied to study the structures in the vicinity of the surface in cross-sectional catalyst samples. In both Pt and Pt-Pd catalysts, the supporting washcoat of a fresh sample looked similar. Noble metal particles

could be found within small-sized Al, Ce, Zr and Si oxide particles. In addition, there were distinct regions of nanocrystalline alumina and amorphous silica. Platinum and palladium were observed to form joint clusters, their size being well below 5 nm. In the platinum catalyst, platinum was detected as irregularly shaped and spherical clusters, sized from 5 to 10 nm. After LPW and HPW treatments, phosphorus was seen to accumulate everywhere, but largest coverages were seen in the alumina regions without noble metals, whereas the smallest concentrations were detected in the silica areas. Structure of the alumina regions changed from nanocrystalline to amorphous, possibly indicating $AlPO_4$ formation. In addition, Pt-Pd clusters were observed to grow and the irregular shapes of Pt clusters to vanish. In the treated samples, the structures became also denser, which is in line with BET and BJH results that indicated decrease in active surface areas and pore volumes. The behaviour of both catalysts as observed with TEM was qualitatively similar, and the main differences between the effects of LPW and HPW treatments were the amount of phosphorus and the extent of structural changes.

Catalyst activity was tested by monitoring conversion of carbon monoxide, propene and several nitrogen oxides. In general, the Pt catalyst was more efficient than the Pt-Pd one, which is possibly due to the beneficence of platinum being metallic. In fresh catalysts, CO oxidation starts already below 110 °C. LPW treatment does not have drastic effects on either of the catalysts, although it increases the light-off temperature of C_3H_6. HPW treatment is significantly more efficient, as it drops the maximum conversion rates below 100 %, excluding CO oxidation on the Pt catalyst. It even prevents NO oxidation on the Pt-Pd catalyst altogether.

3.4.2 Alumina supported platinum-palladium natural gas oxidation catalysts

A similar set of experiments has been carried out to the Pt-Pd/Al_2O_3 NGO catalyst after similar LPW and HPW treatments. Again, phosphorus concentration was measured with ICP-OES and XPS. In LPW and HPW treated samples the former technique gave 3.0 and 5.5 wt.%, and the latter 11 and 13 wt.% (inlet), respectively. With SEM and EDS phosphorus content was observed to decrease linearly as a function of distance from the surface. Thus, the discrepancy between XPS and ICP-OES results is explained by the surface sensitivity of XPS. At the outlet end, phosphorus concentration was found to be significantly smaller with XPS after both

treatments, indicating selective adsorption. Figure 3.16a shows phosphorus 2s spectra taken at the inlet end of the samples. The binding energies indicate phosphate compounds [80]. This is verified by XRD which showed a line for aluminum phosphate.
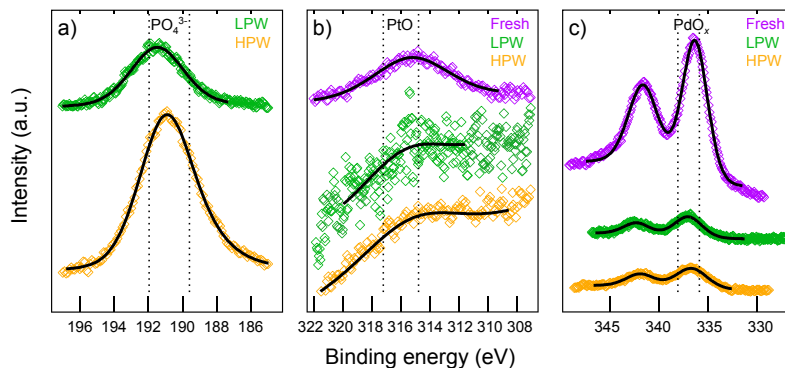
Figure 3.16. (a) P 2s, (b) Pt $4d_{5/2}$ and (c) Pd 3d photoelectron lines measured at the inlet ends of fresh and phosphorus poisoned alumina-supported platinum-palladium natural gas oxidation catalysts. The dashed lines represent boundaries of the binding energy ranges of the marked chemical states.

Figures 3.16b-c show the Pt $4d_{5/2}$ and Pd 3d spectra from the inlet ends. Both noble metals appeared as oxides, and treatments did not have effect on the chemical states. Platinum is most likely PtO, but palladium may be a mixture of different oxidation states [80–82]. With XRD, some of the palladium was seen to be reduced into metallic in the HPW treated sample. This was not seen in XPS at all. A justified explanation is that the surface-most Pt-Pd particles have only palladium oxides, since palladium tends to oxidize in atmospheric conditions. Pt-Pd clusters deeper in the bulk may contain also metallic palladium, but XPS is not capable of detecting them.

TEM showed the washcoat being nanocrystalline γ-alumina, and the size of the dispersed Pt-Pd particles was below 5 nm in a fresh catalyst. The effect of phosphorus was studied by comparing this to the HPW treated catalyst. The treatment changed the alumina washcoat mainly into an amorphous form, which may also predict phosphate formation. The noble metal clusters were seen to increase, being roughly 5 nanometres. Moreover, the structure was generally more dense in the treated sample. This is in line with BET and BJH analyses which implied decrease of the catalyst porosity. Both the active surface area and the pore volume reduced 15% due to the LPW and 30% due to the HPW treatment.

Catalyst activity and poisoning were studied by measuring carbon monox-

ide and methane conversions. CO oxidation was seen to be efficient, a full conversion rate being achieved at not higher than 150 °C while using fresh or LPW treated catalysts. The HPW treatment increased the light-off temperature, but a 100% conversion was gained nevertheless at 250 °C. CH_4 oxidation was weaker already over the fresh catalyst, and the poisoning effect was more drastic. While 600 °C was required to achieve a 100% conversion rate with the fresh catalyst, after the LPW and HPW treatments, maximum rates of 86% and 63% could be gained, respectively.

3.4.3 Silica-zirconia supported platinum diesel oxidation catalysts

Poisoning effect of phosphorus and sulfur, separately and combined, was studied on a Pt/SiO_2-ZrO_2 DOC. The catalyst was exposed to SW, HPW (called PW in Publication VII) and PSW treatments and studied with the aforementioned techniques. Figures 3.17a-b show P 2s and S 2p photoelectron lines from the inlet ends. Phosphorus concentration was 7.9 and 4.0 wt.% at the inlet ends of HPW and PSW treated samples, respectively. Outlet ends showed somewhat smaller concentrations, namely 6.6 and 1.9 wt.%. This is in line with SEM-EDS results indicating ca. 5 wt.% phosphorus content throughout the sample. XPS showed that phosphorus appears again as phosphate (PO_4^{3-}) compounds [80]. Sulfur concentration did not seem to depend on which sample end was measured, being less than 1 wt.% all over the SW treated sample with both XPS and SEM-EDS. In the PSW treated catalyst, sulfur could hardly be detected with XPS. According to XPS, sulfur is part of sulfate (SO_4^{2-}) compounds [80,81].

Platinum $4d_{5/2}$ spectra are presented in figure 3.17c, acquired again at the inlet ends, the outlet spectra being virtually identical. Platinum was metallic in all samples, and its concentration was always found to be around 0.5 wt.%. [82]

Tentative TEM studies indicated no large morphological changes due to the chemical treatments. The washcoat was observed to have separate fine grained silica areas and coarser zirconia regions, platinum clusters being mainly found on the latter. Platinum units did not grow due to the treatments, but porosity of the washcoat decreased, as shown by BET and BJH analyses. The SW treatment had only a mild effect, but in the HPW treated samples the active surface area and the pore volume reduced 39 and 22 percent, respectively, whereas the PSW treatment decreased them
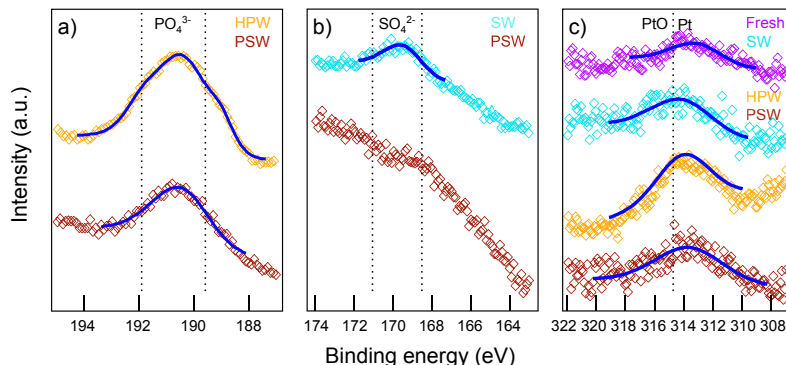
Figure 3.17. (a) P 2s, (b) S 2p and (c) Pt $4d_{5/2}$ photoelectron lines measured at the inlet ends of fresh and phosphorus and sulfur poisoned silica-zirconia-supported platinum diesel oxidation catalysts. The dashed lines represent boundaries of the binding energy ranges of the marked chemical states.

even 74 and 51%.

Activity tests on CO and C_3H_6 oxidation showed that the fresh Pt-SiO_2-ZrO_2 catalyst is not as efficient as a Pt-Al_2O_3 catalyst, light-off temperatures being higher. However, 100% conversions were achieved above 200 °C. The SW treatment did not have a significant effect on the activity, which is understandable because of negligible sulfur concentration. The HPW treatment increased the light-off temperatures of CO and C_3H_6 for 30 and 45 °C, but the poisoning effect by the PSW treatment was weaker. This is in line with XPS measurements showing lower phosphorus concentrations after PSW treatments. The results indicate less efficient phosphorus intake when it needs to compete for the adsorption sites with sulfur.

4. Summary

The main objective of this work was to study the reactions of phosphorus on platinum surfaces. The motivation behind this was in combustion emission control, since platinum is a catalyst employed extensively in automotive catalytic converters, and phosphorus is an effective catalyst poison. To examine the phenomenon of poisoning from a more versatile perspective, both actual catalytic converter materials and single crystal model catalysts were studied. This enabled studying both reactions between catalytic metals and catalyst poisons, and effects the poisons actually have on industrially manufactured catalyst products. In addition, the study of maleic anhydride molecules on a platinum surface was also included in the work, as maleic anhydride can be utilized in biofuel manufacturing processes and thus fits well in the theme of emission control.

Molecular phosphorus was deposited on Pt(111) in Publication II and on Pt(110) in Publication III with CVD in UHV. On both surfaces, increasing tempreture increased also phosphorus intake, indicating activated chemisorption. Furthermore, adsorption terminated at exposures large enough on both surfaces, but the saturation coverage was significantly larger on Pt(110). This is probably due to the surface geometry, the (110) facet being less stable and more active. Moreover, phosphorus formed large clusters on both surfaces. This is not surprising, as phosphorus is known to form solid polymeric meshes, and large clusters have also been proposed in computational studies [83,84]. However, the saturation structure on Pt(110) did not feature large phosphorus clusters but probably a multilayer of smaller units which was not obserbed on Pt(111). These are among the first studies of atomic structures of phosphorus on metal surfaces, and probably the first to use solid red phosphorus as a precursor. They show that phosphorus can react directly with platinum, and its poisoning effect can be severe. Besides the field of automotive catalysis,

studies of phosphorus on single crystal surfaces may draw more attention in the future, if advances are made in epitaxial growth of phosphorene, a semiconducting bilayer of black phosphorus, although this has proven to be an immensely challenging task [85–87].

Phosphorus poisoning of alumina-supported Pt and Pt-Pd DOC's was studied in Publication IV and Publication V. While these types of catalysts have been well-established for a relatively long period, phosphorus poisoning has not been studied extensively. In these studies, the poisoning effect was found to be quite drastic. The phosphorus appeared in the feedstock as phosphate, remaining so after adsorption and binding most prominently with aluminum in the support. Similar treatments carried out on a platinum DOC with a less common silica-zirconia support were seen to result in a slightly more moderate effect on conversion rates in Publication VII. Silica is known to be resistant to sulfur poisoning, which was verified also in this study. On the other hand, there are probably no preceding reports on phosphorus poisoning of a silica-zirconia-supported DOC. The result that co-adsorption of sulfur actually diminishes the poisoning effect of phosphorus is particularly interesting.

Phosphorus poisoning of an alumina-supported Pt-Pd NGO catalyst was the topic of Publication VI. Compared to petroleum, natural gas vehicle industry is of course still in its infancy, but NGO catalysts have already been studied quite extensively. The effect of phosphorus however is not fully understood at the moment. In this study, it was found that phosphorus is really efficient at decreasing methane conversion rates by blocking the surface, forming compounds with the support and apparently inducing Pd reduction. All the effects were due to chemical poisoning, as thermal deactivation has been observed to take place only at higher temperatures in another study [88].

The poisoning effect of phosphorus was found to be strong in both exhaust gas catalyst and single crystal studies. Phosphorus was observed to undermine CO oxidation on all measured exhaust catalyst samples and to prevent CO adsorption on Pt(111). Furthermore, phosphorus also induced morphological changes for the Pt and Pt-Pd nanoparticles on the DOC and NGO catalyst samples and caused reconstructions on Pt(110). However, a single crystal surface is a significantly simpler system than a real catalyst material, and studying a catalyst poison adsorption on a metallic single crystal does not take into account the interactions between the poison and the support, for instance.

In Publication I maleic anhydride was adsorbed on Pt(111) at 170 K as a multilayer. The majority of it desorbs molecularly already below 240 K. At higher temperatures, intact molecules cannot be detected any longer, but fragments of maleic anhydride were seen to desorb in wide temperature ranges up to 600 K. Earlier, maleic anhydride reactions have been studied on various other single crystal surfaces, such as Pd(111), Mo(110) and TiO_2(001) [89–91]. Furthermore, related molecules on Pt(111) have also been studied before [92, 93]. The findings in Publication I are in agreement with the previous reports, although different substrates give rise to differences, such as variations in reaction temperatures and dissociation products.

To conclude, the studies reported in this work provide new information on reactions of phosphorus and maleic anhydride molecules as well as phosphate and sulfate compounds on several different platinum surfaces. Although the motivation lies in emission control, the studies involving single crystal model catalysts are also examples of fundamental surface science, where the results are intended to increase the general knowledge as much as to give rise to new applications. On the other hand, the studies of real catalyst materials are more directly aimed at developing more efficient and durable catalytic converters.

References

[1] K. Oura, V. G. Lifshits, A. A. Saranin, A. V. Zotov, and M. Katayama, *Surface Science – An Introduction*. Springer, 2003.

[2] J. N. Armor, "A history of industrial catalysis," *Catalysis Today*, vol. 163, pp. 3–9, 2011.

[3] W. Yu, M. D. Porosoff, and J. G. Chen, "Review of Pt-based bimetallic catalysis: From model surfaces to supported catalysts," *Chemical Reviews*, vol. 112, pp. 5780–5817, 2012.

[4] N. M. Marković, T. J. Schmidt, V. Stamenković, and P. N. Ross, "Oxygen reduction reaction on Pt and Pt bimetallic surfaces: A selective review," *Fuel Cells*, vol. 1, pp. 105–116, 2001.

[5] R. J. Farrauto and R. M. Heck, "Catalytic converters: State of art and perspectives," *Catalysis Today*, vol. 51, pp. 351–360, 1999.

[6] S. M. Park, H.-G. Jang, E. S. Kim, H.-S. Han, and G. Seo, "Incorporation of zirconia onto silica for improved Pt/SiO_2 catalysts for the selective reduction of NO by H_2," *Applied Catalysis A: General*, vol. 427-428, pp. 155–164, 2012.

[7] R. M. Heck and R. J. Farrauto, "Automobile exhaust catalysts," *Applied Catalysis A: General*, vol. 221, pp. 443–457, 2001.

[8] D. A. Lashof and D. R. Ahuja, "Relative contributions of greenhouse gases to global warming," *Nature*, vol. 344, pp. 529–531, 1990.

[9] J. K. Lampert, M. S. Kazi, and R. J. Farrauto, "Palladium catalyst performance for methane emissions abatement from lean burn natural gas vehicles," *Applied Catalysis B: Environmental*, vol. 14, pp. 211–223, 1997.

[10] P. Castellazzi, G. Groppi, and P. Forzatti, "Effect of Pt/Pd ratio on catalytic activity and redox behavior of bimetallic $Pt–Pd/Al_2O_3$ catalysts for CH_4 combustion," *Applied Catalysis B: Environmental*, vol. 303-311, p. 95, 2010.

[11] P. Gélin and M. Primet, "Complete oxidation of methane at low temperature over noble metal based catalysts: A review," *Applied Catalysis B: Environmental*, vol. 39, pp. 1–37, 2002.

[12] C. T. Goralski Jr. and W. F. Schneider, "Analysis of the thermodynamic feasibility of NO_x decomposition catalysis to meet next generation vehicle NO_x emissions standards," *Applied Catalysis B: Environmental*, vol. 37, pp. 263–277, 2002.

[13] A. Russell and W. S. Epling, "Diesel oxidation catalysts," *Catalysis Reviews*, vol. 53, pp. 337–423, 2011.

[14] D. G. Streets and S. T. Waldhoff, "Present and future emissions of air pollutants in China: SO_2, NO_x and CO," *Atmospheric Environment*, vol. 34, pp. 363–374, 2000.

[15] T. J. Wallington, E. W. Kaiser, and J. T. Farrell, "Automotive fuels and internal combustion engines: A chemical perspective," *Chemical Society Reviews*, vol. 35, pp. 335–347, 2006.

[16] A. K. Neyestanaki, F. Klingstedt, T. Salmi, and D. Y. Murzin, "Deactivation of postcombustion catalysts, a review," *Fuel*, vol. 83, pp. 395–408, 2004.

[17] C. H. Bartholomew, "Mechanisms of catalyst deactivation," *Applied Catalysis A: General*, vol. 212, pp. 17–60, 2001.

[18] P. Forzatti and L. Lietti, "Catalyst deactivation," *Catalysis Today*, vol. 52, pp. 165–181, 1999.

[19] H. S. Gandhi, G. W. Graham, and R. W. McCabe, "Automotive exhaust catalysis," *Journal of Catalysis*, vol. 216, pp. 433–442, 2003.

[20] C. Sedlmair, K. Seshan, A. Jentys, and J. A. Lercher, "Studies on the deactivation of NO_x storage-reduction catalysts by sulfur dioxide," *Catalysis Today*, vol. 75, pp. 413–419, 2002.

[21] M. J. Rokosz, A. E. Chen, C. K. Lowe-Ma, A. V. Kucherov, D. Benson, M. C. P. Peck, and R. W. McCabe, "Characterization of phosphorus-poisoned automotive exhaust catalysts," *Applied Catalysis B: Environmental*, vol. 33, pp. 205–215, 2001.

[22] N. Tian, Z.-Y. Zhou, and S.-G. Sun, "Platinum metal catalysts of high-index surfaces: From single-crystal planes to electrochemically shape-controlled nanoparticles," *Journal of Physical Chemistry C*, vol. 112, pp. 19801–19817, 2008.

[23] H. Steininger, S. Lehwald, and H. Ibach, "On the adsorption of CO on Pt(111)," *Surface Science*, vol. 123, pp. 264–282, 1982.

[24] E. L. Garfunkel, M. H. Farias, and G. A. Somorjai, "The modification of benzene and carbon monoxide adsorption on platinum(111) by the coadsorption of potassium or sulfur," *Journal of the American Chemical Society*, vol. 107, pp. 349–353, 1985.

[25] J. G. Forbes, A. J. Gellman, J. C. Dunphy, and M. Salmeron, "Imaging of sulfur overlayer structures on the Pd(111) surface," *Surface Science*, vol. 279, pp. 68–78, 1992.

[26] H. P. Bonzel and R. Ku, "Adsorbate interactions on a Pt(110) surface. I. Sulfur and carbon monoxide," *Journal of Chemical Physics*, vol. 58, pp. 4617–4624, 1973.

[27] L. Peralta, Y. Berthier, and M. Huber, "Study of the sulphur adsorption on a palladium (110) surface by LEED and AES," *Surface Science*, vol. 104, pp. 435–447, 1981.

[28] S. Wilke and M. Scheffler, "Mechanism of poisoning the catalytic activity of Pd(100) by a sulfur adlayer," *Physical Review Letters*, vol. 76, pp. 3380–3383, 1996.

[29] H. Gutleben and E. Bechtold, "Desorption of sulfur from Pt(100)," *Surface Science*, vol. 191, pp. 157–173, 1987.

[30] A. F. Carley, P. R. Davies, R. V. Jones, K. R. Harikumar, G. U. Kulkarni, and M. W. Roberts, "The structure of sulfur adlayers at Cu(110) surfaces: An STM and XPS study," *Surface Science*, vol. 447, pp. 39–50, 2000.

[31] L. V. Goncharova, S. K. Clowes, R. R. Fogg, A. V. Ermakov, and B. J. Hinch, "Phosphine adsorption and the production of phosphide phases on Cu(001)," *Surface Science*, vol. 515, pp. 553–566, 2002.

[32] X. Zhang, A. Linsebigler, U. Heiz, and J. T. Yates Jr., "Phosphine chemistry on Mo(110) and oxidized Mo(110)," *Journal of Physical Chemistry*, vol. 97, pp. 5074–5079, 1993.

[33] C. M. Greenlief, R. I. Hegde, and J. M. White, "Phosphine and its coadsorption with D_2O on Rh(100)," *Journal of Physical Chemistry*, vol. 89, pp. 5681–5685, 1985.

[34] G. Mitchell, M. Henderson, and J. White, "The adsorption of PH_3 on Pt(111) and its influence on coadsorbed CO," *Surface Science*, vol. 191, pp. 425–448, 1987.

[35] J. Mostany, P. Martínez, V. Climent, E. Herrero, and J. M. Feliu, "Thermodynamic studies of phosphate adsorption on Pt(1 1 1) electrode surfaces in perchloric acid solutions," *Electrochimica Acta*, vol. 107, pp. 349–353, 2009.

[36] R. Gisbert, G. García, and M. T. M. Koper, "Adsorption of phosphate species on poly-oriented Pt and Pt(1 1 1) electrodes over a wide range of pH," *Electrochimica Acta*, vol. 55, pp. 7961–7968, 2010.

[37] M. Weber, F. C. Nart, and I. R. de Moraes, "Adsorption of phosphate species on Pt(111) and Pt(100) as studied by in situ FTIR spectroscopy," *Journal of Physical Chemistry*, vol. 100, pp. 19933–19938, 1996.

[38] K. Sagisaka, M. Marz, D. Fujita, and D. Bowler, "Adsorption of phosphorus molecules evaporated from an InP solid source on the Si(100) surface," *Physical Review B*, vol. 87, p. 155316, 2013.

[39] L. Vitali, M. G. Ramsey, and F. P. Netzer, "Trimer adatom structure of phosphorus on Ge(111)," *Physical Review B*, vol. 63, p. 165320, 2001.

[40] J. Shan, Y. Wang, and R. J. Hamers, "Adsorption and dissociation of phosphine on Si(001)," *Journal of Physical Chemistry*, vol. 100, pp. 4961–4969, 1996.

[41] R. Miotto, A. C. Ferraz, and G. P. Srivastava, "First-principles study of the adsorption of PH_3 on Ge(001) and Si(001) surfaces," *Brazilian Journal of Physics*, vol. 32, pp. 392–395, 2002.

[42] O. Warschkow, H. F. Wilson, N. A. Marks, S. R. Schofield, N. J. Curson, P. V. Smith, M. W. Radny, D. R. McKenzie, and M. Y. Simmons, "Phosphine adsorption and dissociation on the Si(001) surface: An ab initio survey of structures," *Physical Review B*, vol. 72, p. 125328, 2005.

[43] L. Kipp, R. D. Bringans, D. K. Biegelsen, J. E. Northrup, A. Garcia, and L. Swartz, "Phosphine adsorption and decomposition on Si(001) 2×1 studied by STM," *Physical Review B*, vol. 52, pp. 5843–5850, 1995.

[44] D. L. Mowery, M. S. Graboski, T. R. Ohno, and R. L. McCormick, "Deactivation of PdO–Al$_2$O$_3$ oxidation catalyst in lean-burn natural gas engine exhaust: Aged catalyst characterization and studies of poisoning by H$_2$O and SO$_2$," *Applied Catalysis B: Environmental*, vol. 21, pp. 157–169, 1999.

[45] N. Nejar, M. Makkee, and M. J. Illán-Gómez, "Catalytic removal of NO$_x$ and soot from diesel exhaust: Oxidation behaviour of carbon materials used as model soot," *Applied Catalysis B: Environmental*, vol. 75, pp. 11–16, 2007.

[46] A. Corma, S. Iborra, and A. Velty, "Chemical routes for the transformation of biomass into chemicals," *Chemical Reviews*, vol. 107, pp. 2411–2502, 2007.

[47] G. Centi, F. Trifirò, J. R. Ebner, and V. M. Franchetti, "Mechanistic aspects of maleic anhydride synthesis from C$_4$ hydrocarbons over phosphorus vanadium oxide," *Chemical Reviews*, vol. 88, pp. 55–80, 1988.

[48] Y. Román-Leshkov, C. J. Barrett, Z. Y. Liu, and J. A. Dumesic, "Production of dimethylfuran for liquid fuels from biomass derived carbohydrates," *Nature*, vol. 447, pp. 982–986, 2007.

[49] D. Briggs and J. T. Grant, eds., *Surface Analysis by Auger and X-ray Photoelectron Spectroscopy*. IM Publications and SurfaceSpectra Ltd., Trowbridge, UK, 2003.

[50] A. M. Venezia, "X-ray photoelectron spectroscopy (XPS) for catalysts characterization," *Catalysis Today*, vol. 77, pp. 359–370, 2003.

[51] F. P. J. M. Kerkhof and J. A. Moulijn, "Quantitative analysis of XPS intensities for supported catalysts," *Journal of Physical Chemistry*, vol. 83, pp. 1612–1619, 1979.

[52] M. P. Seah and W. A. Dench, "Quantitative electron spectroscopy of surfaces: A standard data base for electron inelastic mean free paths in solids," *Surface and Interface Analysis*, vol. 1, pp. 2–11, 1979.

[53] J. H. Scofield, "Theoretical photoionization cross sections from 1 to 1500 keV," Tech. Rep. UCRL–51326, California University, Lawrence Livermore Laboratory, 1973.

[54] T. L. Barr and S. Seal, "Nature of the use of adventitious carbon as a binding energy standard," *Journal of Vacuum Science Technology A: Vacuum Surfaces and Films*, vol. 13, pp. 1239–1246, 1995.

[55] D. A. Shirley, "High-resolution X-ray photoemission spectrum of the valence bands of gold," *Physical Review B*, vol. 5, p. 4709, 1972.

[56] J. C. Fuggle and S. F. Alvarado, "Core-level lifetimes as determined by x-ray photoelectron spectroscopy measurements," *Physical Review A*, vol. 22, p. 1615, 1980.

[57] M. Aronniemi, J. Sainio, and J. Lahtinen, "Chemical state quantification of iron and chromium oxides using XPS: The effect of the background subtraction method," *Surface Science*, vol. 578, pp. 108–123, 2005.

[58] M. Aronniemi, *Development of XPS data analysis and its application to gas sensor and catalyst surface studies*. PhD thesis, Helsinki University of Technology, 2007.

[59] C. L. Hedberg, ed., *Handbook of Auger Electron Spectroscopy*. third ed.

[60] L. H. Germer, "Low-energy electron diffraction," *Physics Today*, vol. 17, pp. 19–23, 1964.

[61] E. G. McRae, "Self-consistent multiple-scattering approach to the interpretation of low-energy electron diffraction," *Surface Science*, vol. 8, pp. 14–34, 1967.

[62] G. Binnig, H. Rohrer, C. Gerber, and E. Weibel, "Tunneling through a controllable vacuum gap," *Applied Physics Letters*, vol. 40, pp. 178–180, 1982.

[63] G. Binnig and H. Rohrer, "Scanning tunneling microscopy," *Helvetica Physica Acta*, vol. 55, pp. 726–735, 1982.

[64] J. Tersoff and D. R. Hamann, "Theory of the scanning tunneling microscope," *Physical Review B*, vol. 31, pp. 805–813, 1985.

[65] P. A. Redhead, "Thermal desorption of gases," *Vacuum*, vol. 12, pp. 203–211, 1962.

[66] P. H. Dawson, ed., *Quadrupole Mass Spectrometry and Its Applications*. Elsevier, 1976.

[67] J. W. Arblaster, "Crystallographic properties of platinum," *Platinum Metals Review*, vol. 41, pp. 12–21, 1997.

[68] H. Niehus, "Analysis of the Pt(110)-(1×2) surface reconstruction," *Surface Science*, vol. 145, pp. 407–418, 1984.

[69] G. L. Kellogg, "Direct observations of the (1×2) surface reconstruction on the Pt(110) plane," *Physical Review Letters*, vol. 55, pp. 2168–2171, 1985.

[70] J. I. Kroschwitz, ed., *Kirk-Othmer Encyclopedia of Chemical Technology*. John Wiley and Sons, 1995.

[71] H. O. Pierson, ed., *Handbook of Chemical Vapor Deposition*. Noyes Publications, second ed., 1995.

[72] G. Kresse and J. Hafner, "Ab initio molecular dynamics for liquid metals," *Physical Review B*, vol. 47, pp. 558–561 (R), 1993.

[73] G. Kresse and J. Furthmüller, "Efficiency of ab-initio total energy calculations for metals and semiconductors using a plane-wave basis set," *Computational Materials Science*, vol. 6, pp. 15–50, 1996.

[74] J. P. Perdew, K. Burke, and M. Ernzerhof, "Generalized gradient approximation made simple," *Physical Review Letters*, vol. 77, pp. 3865–3868, 1996.

[75] K. M. MacKay, R. A. MacKay, and W. Henderson, eds., *Introduction to Modern Inorganic Chemistry*. CRC Press, Cheltenham, UK, sixth ed., 2002.

[76] R. G. Musket, W. McLean, C. A. Colmenares, D. M. Makowiecki, and W. J. Siekhaus, "Preparation of atomically clean surfaces of selected elements: A review," *Applied Surface Science*, vol. 10, pp. 143–207, 1982.

[77] R. Jones and P. R. Briddon, "The ab initio cluster method and the dynamics of defects in semiconductors," *Semiconductors and Semimetals*, vol. 51, pp. 287–349, 1998.

[78] E. Sanville, S. D. Kenny, R. Smith, and G. Henkelman, "Improved grid-based algorithm for bader charge allocation," *Journal of Computational Chemistry*, vol. 28, pp. 899–908, 2007.

[79] J. W. Niemantsverdriet, *Spectroscopy in Catalysis – An Introduction*. Wiley-VCH, third ed., 2007.

[80] "NIST X-ray photoelectron spectroscopy database, version 4.1," 2012.

[81] J. F. Moulder, W. F. Stickle, P. E. Sobol, and K. D. Bomben, eds., *Handbook of X-ray Photoelectron Spectroscopy*. Perkin-Elmer Corporation, 1992.

[82] J. Z. Shyu and K. Otto, "Identification of platinum phases on γ-alumina by XPS," *Applied Surface Science*, vol. 32, pp. 246–252, 1988.

[83] M. Häser, U. Schneider, and Ahlrichs, "Clusters of phosphorus: A theoretical investigation," *Journal of the American Chemical Society*, vol. 114, pp. 9551–9559, 1992.

[84] A. J. Karttunen, M. Linnolahti, and T. A. Pakkanen, "Icosahedral and ring-shaped allotropes of phosphorus," *Chemistry – A European Journal*, vol. 13, pp. 5232–5237, 2007.

[85] L. Li, Y. Yu, G. J. Ye, Q. Ge, X. Ou, H. Wu, D. Feng, X. H. Chen, and Y. Zhang, "Black phosphorus field-effect transistors," *Nature Nanotechnology*, vol. 9, pp. 372–377, 2014.

[86] M. Bathmunkh, M. Bat-Erdene, and J. G. Shapter, "Phosphorene and phosphorene-based materials – prospects for future applications," *Advanced Materials*, vol. 28, pp. 8586–8617, 2016.

[87] J. Guerrero-Sánchez, M. Lopez-Fuentes, F. Sánchez-Ochoa, N. Takeuchi, and G. H. Cocoletzi, "Nitrogen induced phosphorene formation on the boron phosphide (111) surface: A density functional theory study," *RSC Advances*, vol. 6, pp. 108621–108626, 2016.

[88] M. Honkanen, M. Kärkkäinen, T. Kolli, O. Heikkinen, V. Viitanen, L. Zeng, H. Jiang, K. Kallinen, M. Huuhtanen, R. L. Keiski, J. Lahtinen, E. Olsson, and M. Vippola, "Accelerated deactivation studies of the natural-gas oxidation catalyst – Verifying the role of sulfur and elevated temperature in catalyst aging," *Applied Catalysis B: Environmental*, vol. 182, pp. 439–448, 2016.

[89] V. Pallassana, M. Neurock, and G. Coulston, "Towards understanding the mechanism for the selective hydrogenation of maleic anhydride to tetrahydrofuran over palladium," *Catalysis Today*, vol. 50, pp. 589–601, 1999.

[90] C. Xu and D. W. Goodman, "Adsorption and reaction of maleic anhydride on Mo(110), monolayer Pd(111)/Mo(110) and multilayer Pd(111)/Mo(110)," *Langmuir*, vol. 12, pp. 1807–1816, 1996.

[91] J. N. Wilson, D. J. Titheridge, L. Kieu, and H. Idriss, "Reactions of maleic anhydride over TiO_2(001) single crystal surfaces," *Journal of Vacuum Science & Technology A: Vacuum, Surfaces, and Films*, vol. 18, pp. 1887–1892, 2000.

[92] C. M. Horiuchi and J. W. Medlin, "Adsorption and decomposition of γ-butyrolactone on Pd(111) and Pt(111)," *Surface Science*, vol. 604, pp. 98–105, 2010.

[93] C. M. Horiuchi, M. Rangan, B. M. Israel, and J. W. Medlin, "Adsorption and decomposition of 2(5H)-furanone on Pd(111) and Pt(111): Comparison of ring-opening pathways of an unsaturated cyclic ester," *Journal of Physical Chemistry C*, vol. 113, pp. 14900–14907, 2009.

BUSINESS +
ECONOMY

ART +
DESIGN +
ARCHITECTURE

SCIENCE +
TECHNOLOGY

CROSSOVER

DOCTORAL
DISSERTATIONS